

석사학위논문
Master's Thesis

다중표본 압축 센싱을 이용한
초분광비디오 관측 시스템 개발

Multisampling Compressive Video Spectroscopy

2016

전석준 (朴相禹 Jeon, Daniel)

한국과학기술원

Korea Advanced Institute of Science and Technology

석사학위논문

다중표본 압축 센싱을 이용한
초분광비디오 관측 시스템 개발

2016

전석준

한국과학기술원

전산학부

다중표본 압축 센싱을 이용한 초분광비디오 관측 시스템 개발

전 석 준

위 논문은 한국과학기술원 석사학위논문으로
학위논문 심사위원회의 심사를 통과하였음

2016년 6월 2일

심사위원장 김 민 혁

심 사 위 원 박 진 아

심 사 위 원 윤 성 의

Multisampling Compressive Video Spectroscopy

Daniel Jeon

Advisor: Kim, Min Hyuk

A dissertation submitted to the faculty of
Korea Advanced Institute of Science and Technology in
partial fulfillment of the requirements for the degree of
Master of Science in Computer Science

Daejeon, Korea
June 2, 2016

Approved by

Kim, Min Hyuk
Professor of Computer Science

The study was conducted in accordance with Code of Research Ethics¹.

¹ Declaration of Ethical Conduct in Research: I, as a graduate student of Korea Advanced Institute of Science and Technology, hereby declare that I have not committed any act that may damage the credibility of my research. This includes, but is not limited to, falsification, thesis written by someone else, distortion of research findings, and plagiarism. I confirm that my thesis contains honest conclusions based on my own careful research under the guidance of my advisor.

MCS
20144546

전석준. 다중표본 압축 센싱을 이용한 초분광비디오 관측 시스템 개발.
전산학부 . 2016년. 40+iii 쪽. 지도교수: 김민혁. (영문 논문)

Daniel Jeon. Multisampling Compressive Video Spectroscopy. School of
Computing . 2016. 40+iii pages. Advisor: Kim, Min Hyuk. (Text in
English)

초 록

초분광이미징은 세밀한 분광정보를 측정할 수 있는 기술로 기존의 3개의 색상만 측정할 수 있는 RGB 카메라에 비해 더 많은 물질정보를 획득할 수 있다. 하지만 측정해야 하는 정보가 많아지는 만큼 기존의 초분광이미징 기술들은 여러번에 걸쳐서 촬영하거나 해상도를 낮춰서 촬영해야 했다. 초분광 동영상 촬영을 위해서는 한번의 촬영으로 초분광 정보를 측정해야 한다. CASSI 시스템은 압축센싱을 이용해 단일 촬영으로 초분광 이미지를 획득할 수 있었지만 낮은 해상도를 가지고 있다. 본 학위논문에서는 만화경을 이용해 기존의 CASSI 초분광이미징을 발전시킨 시스템을 제안한다. 본 시스템은 입사된 이미지를 산란기를 이용해 중간 이미지를 생성하고 만화경을 이용해 여러개의 이미지로 복제시킨다. 복제된 이미지들로 부터 초분광 이미지를 복원하면 기존의 다중 촬영 방식의 초분광이미징 시스템의 장점을 활용하면서 한번의 촬영으로 초분광 이미지를 구현할 수 있다.

Abstract

The coded aperture snapshot spectral imaging (CASSI) architecture has been employed widely for capturing hyperspectral video. Despite allowing concurrent capture of hyperspectral video, spatial modulation in CASSI sacrifices image resolution significantly while reconstructing spectral projection via sparse sampling. Several multiview alternatives have been proposed to handle this low spatial resolution problem and improve measurement accuracy, for instance, by adding a translation stage for the coded aperture or changing the static coded aperture with a digital micromirror device for dynamic modulation. State-of-the-art solutions enhance spatial resolution significantly but are incapable of capturing video using CASSI. In this paper, we present a novel compressive coded aperture imaging design that increases spatial resolution while capturing 4D hyperspectral video of dynamic scenes. We revise the traditional CASSI design to allow for multiple sampling of the randomness of spatial modulation in a single frame. We demonstrate that our compressive video spectroscopy approach yields enhanced spatial resolution and consistent measurements, compared with the traditional CASSI design.

Contents

Contents	i
List of Figures	iii
Chapter 1. Introduction	1
1.1 Motivation	1
1.2 Scope	2
1.3 Contributions	2
1.4 Thesis Outline	3
Chapter 2. Background	4
2.1 Hyperspectral Imaging	4
2.2 Optics	5
2.2.1 Dispersion	5
2.2.2 Diffraction	5
2.3 Optical Instruments	6
2.3.1 Apochromatic Lens	6
2.3.2 Diffuser	6
2.3.3 Relay Lens	6
2.3.4 First Surface Mirror	7
2.3.5 Kaleidoscope	7
2.3.6 Coded Aperture	8
2.3.7 Prism	8
Chapter 3. Related Work	9
3.1 Spectral or Spatial Scanning Spectroscopy	9
3.1.1 Fundamental Resolution Tradeoff	9
3.1.2 Filter-Based Spectroscopy	9
3.1.3 Pushbroom Spectroscopy	9
3.2 Coded Aperture Snapshot spectral Imaging	10
3.2.1 Snapshot Spectroscopy	10
3.2.2 Multi-Snapshot Spectroscopy	10
3.3 Kaleidoscopic Imaging	11
Chapter 4. Multisampling Compressive Spectroscopy	12
4.1 Compressive Imaging with Multisampling	12

4.2	Spectral Reconstruction	14
Chapter 5.	System Implementation	15
5.1	Kaleidoscopic Imaging in CASSI	15
5.1.1	Geometric Optics	15
5.1.2	View Multiplication	15
5.1.3	Geometric Calibration	15
5.1.4	Dispersion Directions	17
5.2	Radiometric Calibration	17
5.3	Technical Specifications	18
5.3.1	Coded Aperture	18
5.3.2	Spectral Dispersion	19
5.3.3	Diffuse Screen	20
5.3.4	Objective and Relay Lenses	20
Chapter 6.	Results	21
6.1	Reconstruction Accuracy	21
6.2	Multiview Tradeoff	21
Chapter 7.	Discussion and Future Work	31
Chapter 8.	Conclusion	34
	Bibliography	35
	Acknowledgments in Korean	39
	Curriculum Vitae in Korean	40

List of Figures

2.1	Comparison of RGB imaging	4
2.2	Comparison of diffraction patterns	5
2.3	Relay lens	6
2.4	Comparison of a standard surface mirror and a first surface mirror	7
2.5	Number of views created by kaleidoscope	7
4.1	Schematic diagram of our multisampling compressive coded imaging	12
4.2	Optical path in our hyperspectral imager	13
4.3	Formulation of the reconstruction problem	14
5.1	The ratio of image minification	16
5.2	Hardware prototype of our hyperspectral imager	16
5.3	Kaleidoscope holder	16
5.4	Detecting correspondance points from each view	17
5.5	Raw input image captured by prototype	18
5.6	Overcoming the diffraction limit	18
5.7	Measured dispersion coefficients of the prism	19
5.8	Effect of the diffuser	20
6.1	Comparison of hyperspectral images	23
6.2	Comparison of CASSI system and multiview system	24
6.3	Measurements of spectral accuracy	25
6.4	Hyperspectral video footage	26
6.5	Reconstructed hyperspectral video footage	27
6.6	Comparison of single view and multiview system	28
6.7	Hyperspectral video footage	30

Chapter 1. Introduction

1.1 Motivation

Red, green and blue (RGB) imaging is one of the most commonly used color sensing system for photography, because the human visual system measures three color channels by three types of cones. However, important properties of material usually can be found on other channels. For this reason, cameras used in remote sensing or product inspection should be able to distinguish information from light such as infrared (IR) and ultraviolet (UV). A dense spectrum power distribution also provides useful information of objects. Hyperspectral imaging spectroscopy has been practiced broadly to acquire three-dimensional spectral information of scenes. Many different designs of imaging spectroscopy have been proposed and widely used in many fields, e.g., scientific study, product inspection, aerial/satellite imaging, military applications, etc. However, current commercial hyperspectral imaging systems can capture only static scenes. Many applications such as inspection of products on a conveyor belt and observing a biological specimen need a video spectroscopy system to capture dynamic scenes or temporal transitions of the target object.

Spectral imagers are built with two-dimensional imaging sensors. Consequently, there has been a long-lasting tradeoff between the spatial and the spectral resolutions toward *video capability*. For instance, while bandpass filter-based systems [30, 23] can provide a high spatial resolution, their spectral resolution is limited according to the number of filters. Pushbroom spectral imagers such as [18] can provide a high spectral resolution as well as spatial resolution. However, both scanning approaches are limited to static scenes due to temporal scanning and are incapable of *video spectroscopy* of dynamic scenes.

Snapshot-based imaging approaches, such as coded aperture snapshot spectral imaging (CASSI) [45, 9], have been proposed to capture *spectral video* of dynamic scenes. However, the fundamental tradeoff problem remains for CASSI to support only a *very low spatial resolution* of spectral data, compared to conventional trichromatic imagers. Several alternatives for CASSI have therefore been proposed to handle this tradeoff better. Kittle et al. [22] revised the original design [45] with a micro-translation stage of a coded aperture mask, allowing for multiple sampling, and Tsai et al. [43] utilized the same design for temporal modulation for low-resolution video spectroscopy. Several methods meanwhile employ a digital micromirror device (DMD) for using a dynamic mask, rather than a static pattern, to enhance spatial resolution in CASSI [48, 40]. However, these solutions require multiple snapshots and thus are incapable of video spectroscopy. Alternatively, there are several approaches that combine two different types of cameras, a low-resolution hyperspectral camera, and a high-resolution RGB camera, to increase spatial and spectral resolution [19, 4, 50]. However, these systems approximate spectral information indirectly in hyperspectral videos, rather than directly measuring the actual spectrum per pixel. Furthermore, these multi-camera approaches are more costly than conventional single camera solutions.

In this paper, we propose a new approach combining compressive coded imaging and kaleidoscopic imaging, allowing multiple sampling of the compressive codes. A kaleidoscopic imaging configuration has been used to capture multiple views of dynamic scenes or a large number of views efficiently. We build an alternative CASSI system for *video spectroscopy with enhanced spatial resolution*. We developed an optical design that allows for multisampling of compressive coded snapshots. The proposed design

increases the sampling ratio significantly while capturing hyperspectral video on a single image sensor architecture. We reconstruct input into a four-dimensional hyperspectral video (x, y, λ, t) by solving a sparsity-constrained optimization problem with total variation. We demonstrate that the proposed method improves the spatial resolution of compressive coded imaging without sacrificing video capability relative to the traditional CASSI design.

1.2 Scope

A traditional CASSI system shows a low spectral resolution, since there is a tradeoff between the spectral and the spatial resolution due to the nature of compressive sensing. Multishot hyperspectral imaging is a solution to improve the performance of the CASSI system, but multishot methods are unable to capture moving objects.

In this thesis, we propose a hyperspectral imaging system with multi-sampling with an enhanced resolution, compared with the traditional CASSI system. The proposed method focuses on improving the spectral resolution rather than the spatial resolution, since the inaccurate spectral information is a critical problem of hyperspectral imaging. As a single view of duplicated images in our system has a one-ninth resolution, compared with full sensor resolution, the spatial resolution is not increased as the spectral resolution. We compare both spatial and spectral resolutions of our system with traditional CASSI.

We also describe how to setup a hardware prototype for coupling multisampling and compressive imaging using various optical components such as a kaleidoscope and a coded aperture. A kaleidoscope is an essential component for image duplication. However, using a kaleidoscope causes geometric incoherency, vignette, and image resizing problems. We solve these problems by homography transformation, diffuser, and controlling the focal distance of a relay lens. Geometric calibration registers each view to the reference view, which enables multi-view hyperspectral reconstruction. As a spectrum of a pixel is measured as spatial shifting, accurate geometric calibration is important for both spectral and spatial resolutions.

The proposed hyperspectral imaging system takes the advantages of multisampling on compressive sensing, producing a high-resolution hyperspectral imaging. As a kaleidoscope is a low-cost optical component, the system module can be readily adapted to existing CASSI systems. We evaluate the accuracy of spectral power distributions measured by our hyperspectral imaging system with comparisons with a traditional CASSI system.

1.3 Contributions

Our **contributions** are:

- **A novel optical design that enables multisampling for compressive video spectroscopy.** We propose a hyperspectral video system that utilizes a kaleidoscope for multisampling and coded aperture for compressive sensing, and implement as a prototype to validate the design.
- **Providing insights for coupling multisampling and compressive imaging** We propose a single snapshot multisampling method for compressive imaging, and suggest a hardware design for coupling multisampling and compressive imaging.

Most of these contributions have been presented in the following publication:

- **Daniel Jeon**, Inchang Choi, and Min H. Kim, *Multisampling Compressive Video Spectroscopy*, Computer Graphics Forum (Proc. Eurographics 2016), May 12, 2016, 35(2), pp. 467–477.

1.4 Thesis Outline

This thesis is organized as follows. Chapter 2 describes background knowledge about hyperspectral imaging and optical instruments employed in this system. Chapter 3 introduces related works on hyperspectral imaging including single snapshot imaging and multishot imaging. Chapter 4 explains the details of our compressive hyperspectral reconstruction algorithm. Chapter 5 presents the design of our imaging system and calibration processes. Chapter 6 shows the results of the reconstruction. We share remaining issues in our system and potential improvements in Chapter 7. Finally, Chapter 8 concludes this thesis.

Chapter 2. Background

This chapter provides a brief overview of background knowledge.

2.1 Hyperspectral Imaging

Light is electromagnetic radiation in a range of frequency. A human can perceive three color channels out of electromagnetic spectrum through three different types of cones. Likewise, commercial cameras used for digital photography are designed for capturing three channels of a spectrum to mimic human vision system. While three channels of red, green and blue (RGB) are enough for generate visualization to represent a color, it cannot specify characteristics of material. In contrast, hyperspectral imaging can offer dense spectrum information for each pixel in the image. Hyperspectral imaging is related to multispectral imaging. The difference between two imaging systems is the bandwidth of a single channel. Multispectral imaging captures more channels than RGB imaging, but it does not record the full spectrum of an object. Hyperspectral imaging can cover a spectrum range with a finer resolution of 10nm bandwidth than multispectral imaging.

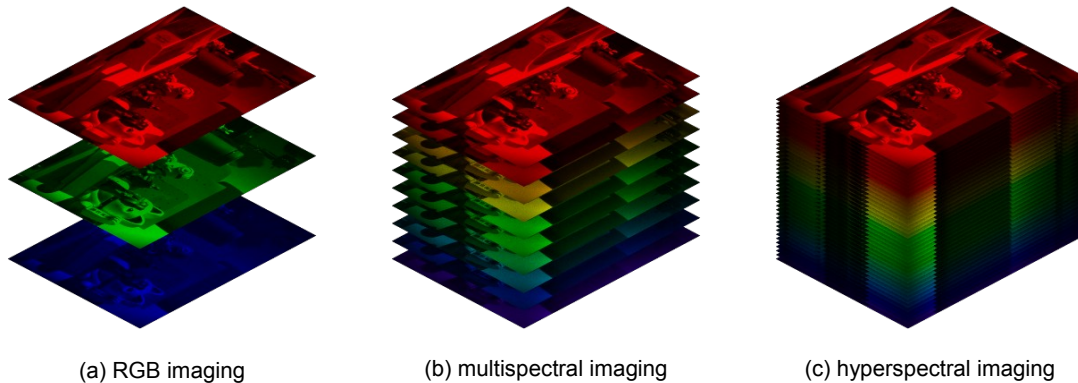


Figure 2.1: Comparison of RGB imaging, multispectral imaging, and hyperspectral imaging.

The advantage of hyperspectral imaging is that no prior knowledge of target object is needed for property analysis because an entire spectrum is acquired at each point. Also, hyperspectral imaging provides relationships among the different spectra in a neighborhood, allowing to discover spectral-spatial models for a more accurate segmentation and classification of the image. The disadvantage of hyperspectral imaging is complexity. Complex optical systems, sensitive detectors, fast computers, and large data storage are needed for measuring and analyzing a hyperspectral image. Since a hyperspectral image has one more axis for wavelength, data size is larger than an RGB image. Also, hyperspectral cube should be transformed to two-dimensional image using an optical system because image sensors can only measure two-dimensional data.

2.2 Optics

2.2.1 Dispersion

In optics, the wavelength of light determines the refractive index. When light passes through a refractive medium, light at each wavelength refracts at a different angle, splitting white light into a rainbow. Dispersion is a phenomenon which separates light depending on wavelength. Two kinds of optical components are commonly used for dispersion: prism and diffraction grating. While a prism refracts light for dispersion, diffraction grating diffracts light. A diffraction grating has higher dispersion power than a prism, and it produces multiple dispersion images, depending on diffraction modes. However, diffraction grating produces overlaps of dispersed light among different modes, and the light efficiency of a diffraction grating is lower than a prism due to multiple diffraction modes.

2.2.2 Diffraction

In classical physics, the diffraction is described as the interference of waves according to the Huygens-Fresnel principle. A diffraction pattern can be observed when light is projected on a plate after passing through a small slit. The diffraction power depends on the size of the slit and the wavelength of light. As imaging systems stop the passage of light using an aperture, diffraction patterns may appear on captured images. The diffraction pattern created by the aperture is called Airy disk, which degrades the quality of an imaging system. The radius of an airy disk can be expressed as

$$R = 1.22 \frac{L\lambda}{d}, \quad (2.1)$$

where L is a distance from the aperture to the sensor plane, λ is the wavelength of light, and d is the diameter of the aperture. The airy pattern can be reduced by increasing the size of pixel pitch or the size of the aperture. On the other hand, diffraction occurs in many optical components such as a diffraction grating and a holographic diffuser. A diffraction grating consists of a series of grooves. Diffraction from multiple slits narrows the peak points of each diffraction mode, causing light to disperse into component wavelength. A holographic diffuser also consists of multiple holes but in a random order. By randomly distributed holes, the diffraction patterns are blurred out. Figure 2.2 shows light intensity distributions of diffraction patterns from a single hole, evenly distributed multiple holes, and randomly distributed multiple holes.

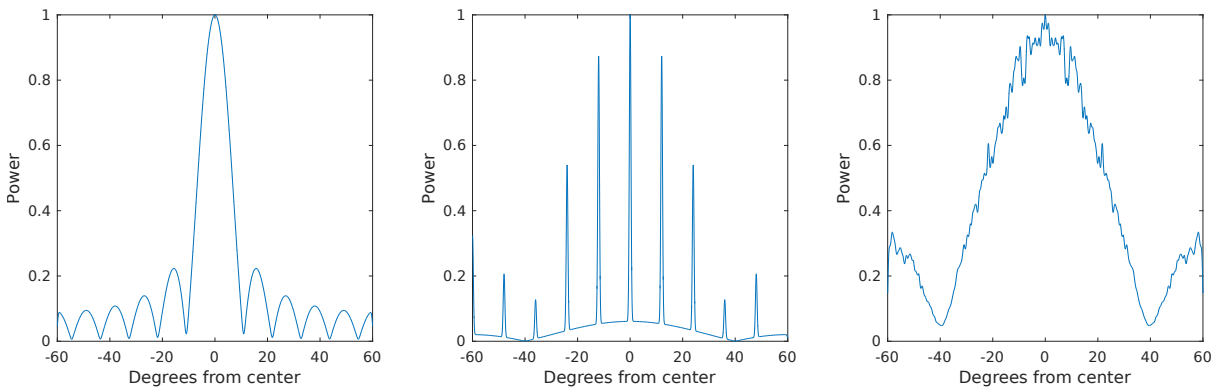


Figure 2.2: Comparison of diffraction patterns from (a) a single slit, (b) evenly distributed multiple slits, and (c) randomly distributed multiple slits.

2.3 Optical Instruments

2.3.1 Apochromatic Lens

Owing to dispersion, incoming rays of all wavelengths cannot converge to a single spot. This problem is called a chromatic aberration. We use an apochromatic lens as an objective lens to prevent the chromatic aberration. The apochromatic lens consists of multiple element lenses with various shapes and refractive indices to minimize chromatic aberration.

2.3.2 Diffuser

A diffuser is an optical component that causes light to spread evenly across a surface. A diffuser is often used as an intermediate imaging medium. Using a translucent diffuser, an observer can see an image on the opposite side of the source. Three types of optical components are used for diffusers including ground glass, opal, and holographic materials. A ground glass is ideal for applications that require low scatter loss, but irregular surface generates noise on a result image. In contrast, opal produces clear result image, but light transmission rate of opal is very low. The holographic diffuser is similar to a diffractive optical element. However, the etching pattern is not uniformly arranged. The random diffraction enables light diffusing with high light efficiency and clear imaging. Since an angle of diffusion is determined by diffraction power, various scattering angles are available by changing hole size of the diffuser.

2.3.3 Relay Lens

A relay lens comprises arrays or imaging lenses placed inside an optical system to deliver an image from the source image plane to the target image plane. Endoscopes and periscopes use a relay lens for the purpose of extending the optical system. A relay lens is useful when a system utilizes multiple optical components for image manipulation. The proposed system contains two relay lenses for two types of image manipulation: image duplication and encoding. Also, the relay lens can resize the image by changing the object and the image distance. However, using the relay lens often creates a severe vignetting problem as shown in Figure 2.3. The problem can be avoided by inserting a convex lens or a diffuser at the intermediate image plane. While a diffuser is more efficient for reducing vignette, it also significantly reduces light transmission.

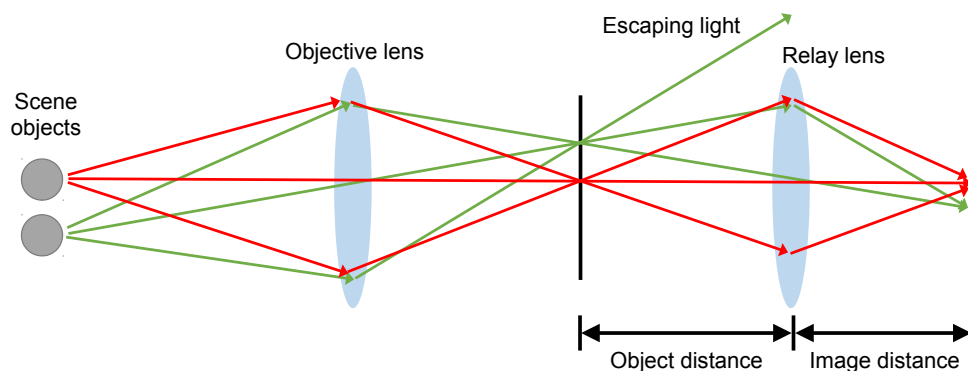


Figure 2.3: A relay lens transfers an image from an image plane to the other plane. The green line shows the vignetting problem caused by light escaping from the system.

2.3.4 First Surface Mirror

A typical mirror is a second surface mirror, in which a reflective layer is placed under the front glass. A second surface mirror has two disadvantages for high precision optics. The first problem is that incident light on the second surface mirror is subject to chromatic dispersion from the substrate material. Moreover, reflection in the substrate produces ghost artifacts. Additional ghost reflections occur as light bounces between a front glass and a reflective glass as shown in Figure 2.4(a). First surface mirror, also known as a front surface mirror, has the reflective layer on the face of the glass to prevent ghost images. The first surface mirror is used in high precision imaging applications such as scanning, projections, telescopes, periscopes, and kaleidoscope. A metal coated mirror is typical first surface mirrors because metallic materials can directly reflect incident light.

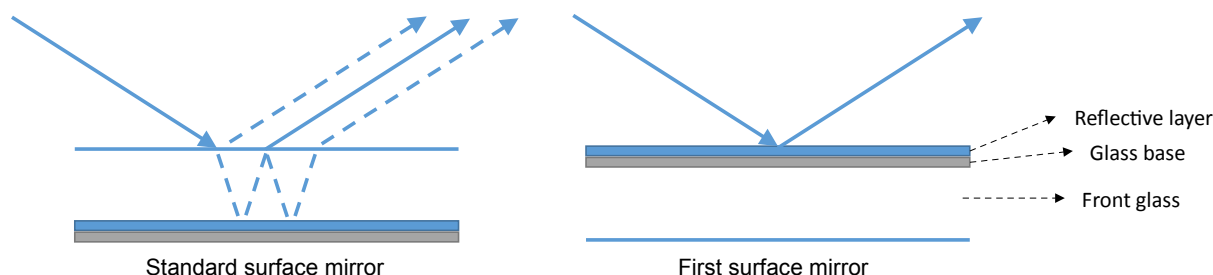


Figure 2.4: Comparison of a standard surface mirror(a) and a first surface mirror(b).

2.3.5 Kaleidoscope

A kaleidoscope is an optical instrument that surrounded by multiple first surface mirrors. Repeated reflection in the mirrors creates multiple identical images with different orientations. Most kaleidoscopes are intended as children's toy, but a kaleidoscope can be utilized for imaging applications that require multiple views. The number of views depends on the focal length of a lens (see Figure 2.5). A more number of views can provide a higher number of sub-images, but the spatial resolution of a single view decreases.

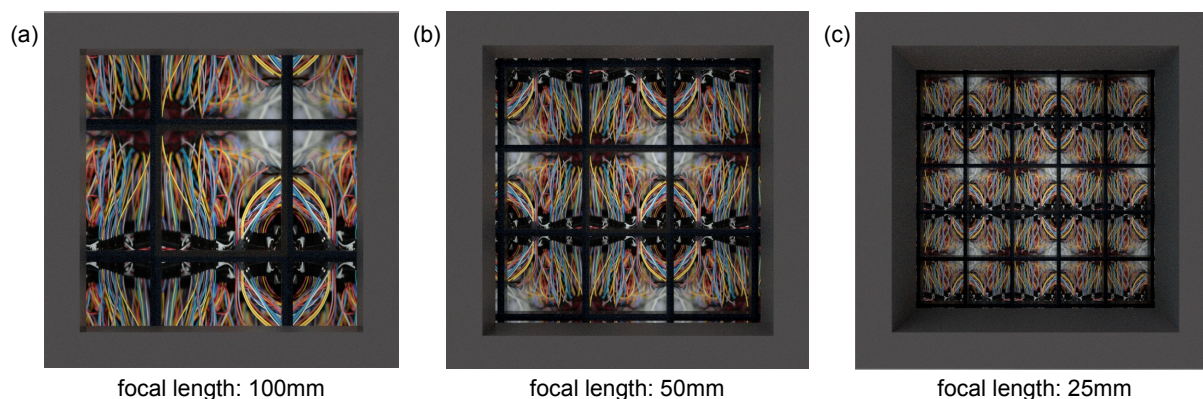


Figure 2.5: A number of views created by a kaleidoscope depends on the focal length of a lens. (a) A camera with a long focal length captures the small number of views. (c) A camera equipped with a lens of a short focal length captures a large number of views.

2.3.6 Coded Aperture

A coded aperture is a glass patterned with grid structure that is opaque to light. Light encoding using the coded aperture enables us to reconstruct input light information. In X-ray imaging, the coded aperture is used as an imaging component, because a normal lens blocks high-frequency light. Also, the coded aperture can be used to obtain additional information from an image such as depth [24].

2.3.7 Prism

A prism is a transparent optical element with flat surfaces that refract light. The flat surfaces have an angle between them. The traditional shape of the prism is triangular, which has a triangular base and rectangular sides. The angle between surfaces is called the apex angle. The relationship between the deviation angle δ of light and the prism apex angle α can be represented as

$$\delta(\lambda) \approx [n(\lambda) - 1]\alpha, \quad (2.2)$$

where λ is the wavelength of light, and $n(\lambda)$ is the refractive index of the material at wavelength λ . The prism is ideal for the dispersion purpose. The power of dispersion depends on the apex angle. A prism with the small apex angle has a weak dispersion power.

Chapter 3. Related Work

Imaging spectroscopy has been researched extensively in recent decades. For brevity's sake, we refer readers to [2] for background and an overview of this subject. Hyperspectral imaging systems can be categorized into either scanning or non-scanning spectroscopy. This section focuses on a survey of non-scanning spectroscopy.

3.1 Spectral or Spatial Scanning Spectroscopy

3.1.1 Fundamental Resolution Tradeoff

Hyperspectral imaging is a spectroscopy technology that captures image information with an additional dimension of spectra. Traditional hyperspectral imaging systems require temporal scanning to reconstruct a three-dimensional spatio-spectral data cube. A hyperspectral imager employs a two-dimensional imaging sensor to capture input. Since the dimensions of the sensor are lower than those of the hyperspectral data cube, a tradeoff between the spatial and the spectral resolution in these systems is inevitable. Diverse optical designs and algorithms have been proposed to better handle this tradeoff of spatio-spectral information. Traditional hyperspectral imagers commonly use a scanning method with a spectral division or spatial division. Scanning methods sacrifice either spectral or spatial resolution to enhance the other resolution.

3.1.2 Filter-Based Spectroscopy

In spectral scanning, each two-dimensional image represents a monochromatic spatial map of a scene. Spectral scanning employs a bandpass-filter to measure a single color channel. Bandpass-filter-based spectroscopy captures a sequence of images with narrow bandpass filters [37] coupled with a monochromatic camera, and reconstructs a hyperspectral image by packing spectral channels. The spectral resolution depends on the number of filters, and the spatial resolution is determined by the resolution of the sensor. Filter-based imaging provides high spatial resolution but with limited spectral resolution. Since multiple channels must be captured via temporal scanning, captured subjects are limited to static objects. Mansouri et al. [31] utilize a rotating wheel with bandpass filters to decrease the capture time. However, the number of bandpass filters is limited to seven due to capturing time and the size of the rotating wheel. In place of the bandpass filter, Hardeberg et al. [17, 33] measured the spectral reflectance using a liquid crystal tunable filter (LCTF) with a monochromatic camera, where the bandwidth of the imager was 10nm. An LCTF-based multi-way camera [23] increases measuring speed, but not enough speed for video spectroscopy.

3.1.3 Pushbroom Spectroscopy

Pushbroom-based systems have been broadly used in many applications for the last decade, particularly in remote sensing. A pushbroom-based system isolates an image into a narrow column through a single slit, disperses each column by a prism or a diffraction grating to mechanically scan optical dispersion, and then packs the column-wise dispersion into a spectral image. The drawbacks of this design are that the

spatial resolution along the mechanically moving axis is lower than that of the other axis direction and that these systems, like filter-based systems, can capture only *static scenes*. The spectral resolution of pushbroom-based systems is, however, higher than that of filter-based systems. The spectral resolution is determined by the number of pixels within the range of spectral dispersion in the sensor. While packing the column-wise dispersion into a spectral image, mechanically moving the slit produces artifacts on a reconstructed image. Pushbroom systems suffer from artifacts that can degrade performance of the classification of pixels and feature identification. Mouroulis et al. [32] proposed a frequency-based reconstruction method to obtain a spatially uniform spectral data cube. Recently, Hoyer et al. [18] presented a system by physically attaching a set of light mixing chambers on the slit to reduce typical artifacts in the pushbroom architecture.

3.2 Coded Aperture Snapshot spectral Imaging

3.2.1 Snapshot Spectroscopy

Compared with the pushbroom- or filter-based systems, snapshot-based systems capture a full 3D spatial-spectral data with a snapshot and are capable of capturing dynamic scenes. Although *snapshot* spectroscopy is capable of hyperspectral video, the technical tradeoff between spatial and spectral resolution remains a severe problem. Snapshot spectroscopy also utilizes dispersion by a prism or a diffraction grating coupled with a coded mask to reconstruct spectral information by decomposing spatial resolution or solving a projection problem.

A four-dimensional imaging spectrometer (4DIS) [13] samples input pixels using pupil array. A snapshot image mapping spectrometer (IMS) [12] transforms a two-dimensional image to a line image using an optical fiber bundle. A computed tomography imaging spectrometer (CTIS) [11] reconstructs a spectral image from several dispersed images with various dispersion power and directions. Du et al. [9] utilized an occlusion mask for pixel sampling. However, these methods sacrifice spatial resolution while they use a part of sensor for spatial sensing and the other area for spectral sensing.

Gehm et al. [14] introduced a pioneering snapshot spectroscopy system, so-called dual-disperser coded aperture snapshot spectral imaging (DD-CASSI), which uses a coded aperture to modulate spectral data. Wagadarikar et al. [46, 47] proposed single-disperser CASSI systems (SD-CASSI) that allow for video spectroscopy. Rajwade et al. [36] developed CASSI system by using a Bayesian implementation of blind compressive sensing. Habel et al. [15] proposed a hyperspectral imager by revising a conventional camera to reconstruct spectral information via computed tomography imaging. The imager is formed with relatively cheap apparatuses while providing up to 4.89 nm spectral resolution (54 spectral bands); its spatial resolution is limited to 120 x 120 pixels. These snapshot-based systems suffer from a lack of spatial resolution due to the aforementioned tradeoff.

3.2.2 Multi-Snapshot Spectroscopy

In order to improve spatial resolution, several alternative designs have been proposed to increase the sampling rate in CASSI. Kittle et al. [22, 20] proposed a multiple snapshot CASSI that captures many snapshots posing a coded mask on a micro translation stage to randomly translate the position of the mask. Wu et al. [53] utilized a DMD as a programmable coded aperture to diversify the random pattern of the coded mask. Furthermore, spatial-spectral encoding allows a higher resolution of hyperspectral images. Lin et al. [25] represented an optical camera design for spatial-spectral encoding using liquid

crystals on silicon. Even though these systems improve the spatial resolution significantly compared to single snapshot approaches, they are incapable of capturing dynamic scenes for hyperspectral video.

Another alternative approach, a dual-camera system with a low-resolution hyperspectral camera and a high-resolution DSLR camera, was proposed [5, 50, 29]. This method propagates low-resolution spectral information to the high-resolution pixel domain from the RGB camera by estimating pixel similarity or a basis that represents reflectance spectra via matrix factorization [19]. However, these high-resolution spectra are approximations rather than direct measurements of actual spectra.

3.3 Kaleidoscopic Imaging

Reshetouski et al. [39] proposed calibration and imaging theory for kaleidoscopic imaging configurations. They then investigated optical geometry in a room of planar mirrors [38]. Planar mirrors have been broadly used in various imaging applications. For instance, a planar mirror system was proposed for multiple views in capturing reflectance functions [16]. Recently, Manakov et al. [30] introduced a filter-based snapshot multispectral imaging system based on a kaleidoscope. The kaleidoscope produces $N \times N$ identical copies of the original image. Each image is filtered by a bandpass-filter with a different wavelength band. We are inspired by this optical design of image duplication, and apply it to *compressive coded aperture snapshot imaging*. Different from Manakov et al.’s approach, we duplicate images with diverse random apertures, allowing for multisampling of compressive coding. To the best of our knowledge, our work is the first to apply kaleidoscopic imaging to compressive coded imaging to achieve high resolution in hyperspectral videos.

Chapter 4. Multisampling Compressive Spectroscopy

We were motivated to capture hyperspectral video with enhanced spatial resolution. We built our CASSI system design from scratch but extended the compressive design toward multiple sampling to enhance the spatial resolution of traditional CASSI without sacrificing video capture capability. We begin by describing the foundations of compressive imaging, followed by our design.

4.1 Compressive Imaging with Multisampling

Let us define the spectral intensity of light in a frame as a function f of wavelengths λ and spatial locations (x, y) . The input image with continuous spectra f , shown on the left in Figure 4.1, is duplicated into k instances of f_k^0 images

$$\mathbf{f} = [f_1^0, f_2^0, \dots, f_k^0],$$

where the initial image f on a diffuse screen is multiplied by four first-surface mirrors. See Section 5.1 for details of optical implementation.

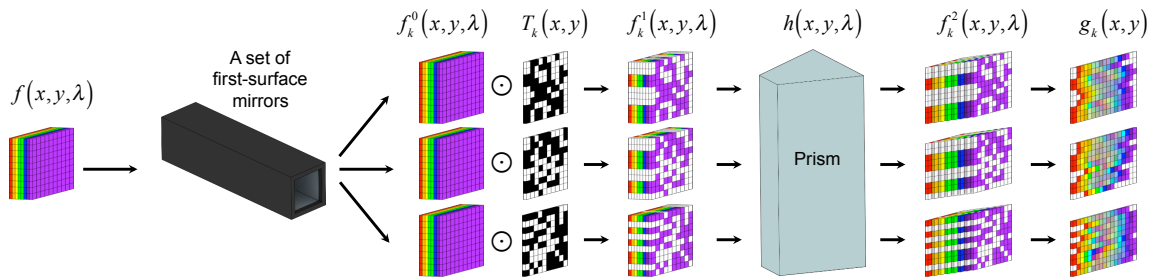


Figure 4.1: Schematic diagram of our multisampling compressive coded imaging. An initial hyperspectral image f passing an objective lens is duplicated by first-surface mirrors and modulated by *different* coded aperture masks $\mathbf{T} = [T_1, T_2, \dots, T_k]$ to coded images $\mathbf{f}^1 = [f_1^1, f_2^1, \dots, f_k^1]$. \mathbf{f}^1 is then dispersed as a shear spectral function $\mathbf{f}^2 = [f_1^2, f_2^2, \dots, f_k^2]$, and projected to a monochromatic sensor $\mathbf{g} = [g_1, g_2, \dots, g_k]$.

Each duplicated image f_k^0 is filtered by a *different* coded aperture transmission function $T_k(x, y)$, respectively. Note that the random mask functions $\mathbf{T} = [T_1, T_2, \dots, T_k]$ are different while the duplicated f_k^0 images are identical. The modulated spectral density function $\mathbf{f}^1 = [f_1^1, f_2^1, \dots, f_k^1]$ via the coded aperture \mathbf{T} is computed by a product:

$$f_k^1(x, y, \lambda) = f_k^0(x, y, \lambda)T_k(x, y) .$$

A prism disperses the duplicated coded images \mathbf{f}^1 along a horizontal axis. The length of dispersion of a wavelength λ can be obtained from the calibration of dispersion as a function of $\phi(\lambda)$, which describes the amount of pixel shift with respect to wavelength λ . We can describe the spectral density f_k^2 after the diffraction grating as

$$\begin{aligned} f_k^2(x, y, \lambda) &= \iint \delta(x' - [x + \phi(\lambda)])\delta(y' - y)f_k^1(x', y', \lambda)dx'dy' \\ &= \iint h(x' - \phi(\lambda), x, y', y, \lambda)f_k^1(x', y', \lambda)dx'dy' , \end{aligned}$$

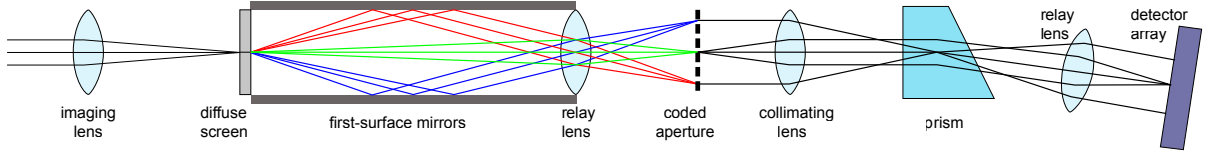


Figure 4.2: Optical path in our hyperspectral imager. An objective lens (left) forms an image on a diffuse screen. This image is duplicated as an array of 3-by-3 images by four first-surface mirrors and projected to a coded aperture (middle). The duplicated images with different coded masks are collimated and transformed to a monochromatic sensor (right) via a prism.

where h describes the two-dimensional dispersion of $\phi(\lambda)$ via the prism as a combined function of two Dirac delta functions $\delta(x' - [x + \phi(\lambda)])\delta(y' - y)$.

The detector array only measures the intensity of the light rather than the spectral density. The intensity of a position (x, y) is integration over a set of wavelengths Λ in the k -th duplication:

$$\begin{aligned} g_k(x, y) &= \int_{\Lambda} \iint h(x' - \phi(\lambda), x, y', y, \lambda) f_k^1(x', y', \lambda) dx' dy' d\lambda \\ &= \int_{\Lambda} \iint h(x' - \phi(\lambda), x, y', y, \lambda) T_k(x, y) \\ &\quad \times f_k^0(x', y', \lambda) dx' dy' d\lambda. \end{aligned} \quad (4.1)$$

Suppose we have an image sensor that pixelates the light intensity as a two-dimensional array of a pixel size Δ . We can rewrite the discrete pixel intensity \mathbf{g} at a position (i, j) in the k -th duplication as:

$$\begin{aligned} \mathbf{g}_{ijk} &= \iint g_k(x, y) \text{rect}\left(\frac{x}{\Delta} - i, \frac{y}{\Delta} - j\right) dx dy, \\ &= \iint \int_{\Lambda} \iint h(x' - \phi(\lambda), x, y', y, \lambda) T_k(x, y) \\ &\quad \times f_k^0(x', y', \lambda) \text{rect}\left(\frac{x}{\Delta} - i, \frac{y}{\Delta} - j\right) dx' dy' d\lambda dx dy. \end{aligned} \quad (4.2)$$

In the same manner, the coded aperture mask $T_k(x, y)$ can be formulated as a set of discrete pinholes $\mathbf{T}_{i'j'k}$ with a pixel size of Δ' :

$$T_k(x, y) = \sum_{i', j'} \mathbf{T}_{i'j'k} \text{rect}\left(\frac{x}{\Delta'} - i', \frac{y}{\Delta'} - j'\right). \quad (4.3)$$

We can substitute $T_k(x, y)$ in Equation (4.2) with Equation (4.3):

$$\begin{aligned} \mathbf{g}_{ijk} &= \sum_{i', j'} \mathbf{T}_{i'j'k} \iint \int_{\Lambda} \iint h(x' - \phi(\lambda), x, y', y, \lambda) \\ &\quad \times \text{rect}\left(\frac{x}{\Delta'} - i', \frac{y}{\Delta'} - j'\right) \\ &\quad \times f_k^0(x', y', \lambda) \text{rect}\left(\frac{x}{\Delta} - i, \frac{y}{\Delta} - j\right) dx' dy' d\lambda dx dy. \end{aligned} \quad (4.4)$$

Now we can rewrite the above equation in a matrix-vector form. Suppose the captured input image of k duplication, is $\mathbf{g} \in \mathbb{R}^{ijk}$. A hyperspectral image function $f_k^0(x', y', \lambda) \text{rect}(\frac{x}{\Delta} - i, \frac{y}{\Delta} - j)$ of k duplication with l number of wavelengths is $\mathbf{f} \in \mathbb{R}^{ijl}$. The projection of the spectral dispersion function $h(x' - \phi(\lambda), x, y', y, \lambda) \text{rect}(\frac{x}{\Delta} - i, \frac{y}{\Delta} - j)$ combined with the compressive coded mask \mathbf{T} can be presented as a non-negative and binary matrix $\mathbf{H} \in \mathbb{R}^{ijkl \times ij l}$. Now we can rewrite the entire process of spectral dispersion and projection as the product of \mathbf{H} and \mathbf{f} :

$$\mathbf{g} = \mathbf{H}\mathbf{f}. \quad (4.5)$$

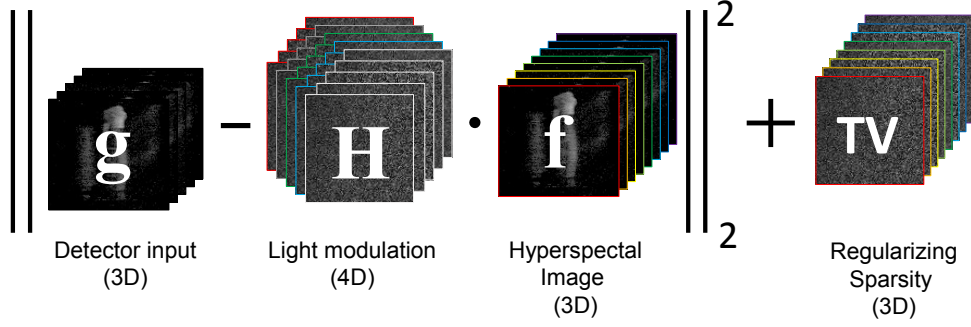


Figure 4.3: Formulation of the reconstruction problem with total variation regularizer.

This matrix \mathbf{H} shears and projects the hyperspectral data cube \mathbf{f} to the sensor array \mathbf{g} . We obtain the matrix \mathbf{H} by registering the mask pattern of each wavelength with its dispersion coefficient measured (see Figure 5.7 in Section 5).

4.2 Spectral Reconstruction

State-of-the-art CASSI systems find an optimal solution to the ill-posed inverse problem of reconstructing input spectra by using an expectation maximization with total variation [14, 45, 22, 53] or learning an over-complete dictionary via sparse representation [26, 25, 35, 50, 41]. The foundation of our reconstruction workflow follows the traditional reconstruction of CASSI using a total variation (TV) regularizer. Our reconstruction problem of multisampling hyperspectral channels is to seek \mathbf{f} that can minimize $\|\mathbf{g} - \mathbf{H}\mathbf{f}\|_2^2$. We formulate the reconstruction as a Lagrangian relaxation problem of a constrained optimization:

$$\min_{\mathbf{f}} \frac{1}{2} \|\mathbf{g} - \mathbf{H}\mathbf{f}\|_2^2 + \tau\Gamma(\mathbf{f}), \quad (4.6)$$

where τ is set to around 0.1 in our experiments. We solve this data term with the TV-L1 regularizer. Figure 4.3 visualizes each variable. We compute an isotropic L1 norm $\Gamma(\mathbf{f})$ of variation in the horizontal and the vertical axis of the spectral data cube [1]:

$$\begin{aligned} \Gamma(\mathbf{f}) = & \sum_l \sum_{i,j} \{|\mathbf{f}(i+1, j, l) - \mathbf{f}(i, j, l)| \\ & + |\mathbf{f}(i, j+1, l) - \mathbf{f}(i, j, l)|\}. \end{aligned} \quad (4.7)$$

Since the L1 norm is known to be robust, and it enforces the sparsity of the gradients of \mathbf{f} , we select the L1 norm over the L2 norm to find a robust and smooth solution. We sum the spatial variations of the horizontal and vertical axes within the spectral data cube. Note that while calculating the total variation, spatial smoothness is considered explicitly without spectral smoothness, thereby allowing steep gradient changes along the spectral axis.

Chapter 5. System Implementation

This chapter describes technical details for implementing our system prototype of 4D hyperspectral video spectroscopy.

5.1 Kaleidoscopic Imaging in CASSI

5.1.1 Geometric Optics

The design of our system originates from a single disperser architecture with a coded aperture of CASSI proposed by Wagadarikar [45]. Figure 4.2 shows a schematic diagram of light transport in our system. A conventional objective lens forms an image on a diffuse screen, which is surrounded by four first-surface mirrors to duplicate the image. The duplicated images are then relayed to a coded aperture mask for spatial modulation. The compressed rays are collimated to be dispersed by a prism. Note that the collimating step should be placed prior to the dispersion to avoid inconsistent focusing among wavelengths. The last relay lens focuses the dispersed light on an image sensor. The captured light is the projection of the sheared spectrum of a scene (refer to Section 4.1). In summary, our novel optical design with image duplication allows for *multiple sampling* of randomness of the coded aperture to enhance spatial resolution with benefits of compressive coded aperture snapshot imaging for video spectroscopy.

5.1.2 View Multiplication

Once an objective lens forms an image on a diffuse screen, four surrounding first-surface mirrors duplicate the image on a virtual plane at the same focusing distance parallel to the diffuser. The duplicated 3×3 views of the diffuser are then compressed to the size of the image sensor. The minification ratio of copied images $m = l_b/l_a$ is determined by the horizontal length of the mirrors a and the focal length f of the relay lens (see Figure 5.1):

$$m = \frac{b}{a} = \frac{1}{a/f - 1} \quad \text{s.t.} \quad \frac{1}{a} + \frac{1}{b} = \frac{1}{f}.$$

For image multiplication, we build a four-sided kaleidoscope in dimensions of $24 \times 24 \times 240$ mm with four first-surface mirrors from Edmund Optics and a mirror holder created by a 3D printer. Figure 5.3 shows a 3D model of our mirror holder design. The holder consists of four grooves to hold mirrors. We attach two holders at the end of mirrors to make the kaleidoscope rigid.

5.1.3 Geometric Calibration

Misalignment of the mirrors introduces perspective distortion of copied images. To solve the misalignment problem, we performed geometric calibration on captured views, following Manakov et al. [30]. Capturing a checkerboard on the imaging plane of the objective lens allows us to find correspondence points as shown in Figure 5.4. Using correspondence pairs, we estimate homographies between duplicated views and the original view using the corresponding pairs of the checkerboard. By warping the copied views with the estimated homographies, all views can be aligned with respect to center view coordinates. This geometric calibration is independent of the scene because optical distortion occurs after objective image formation.

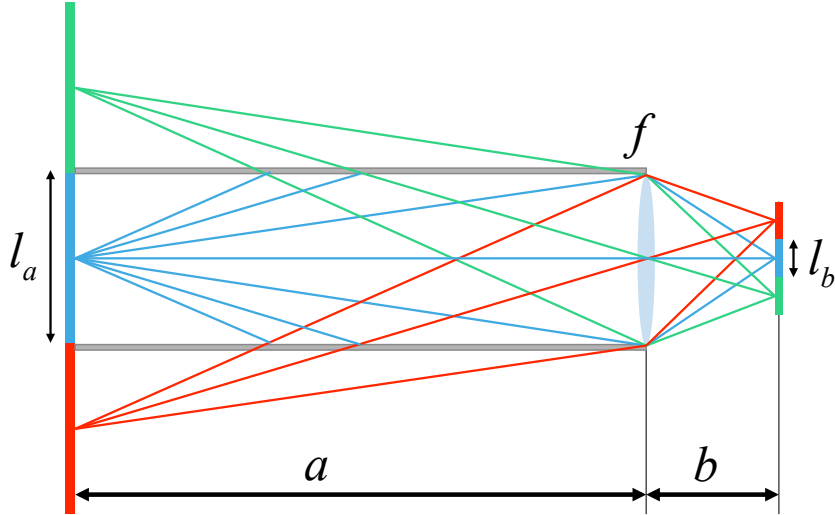


Figure 5.1: The ratio of image minification is determined by the object distance a and focal length b .

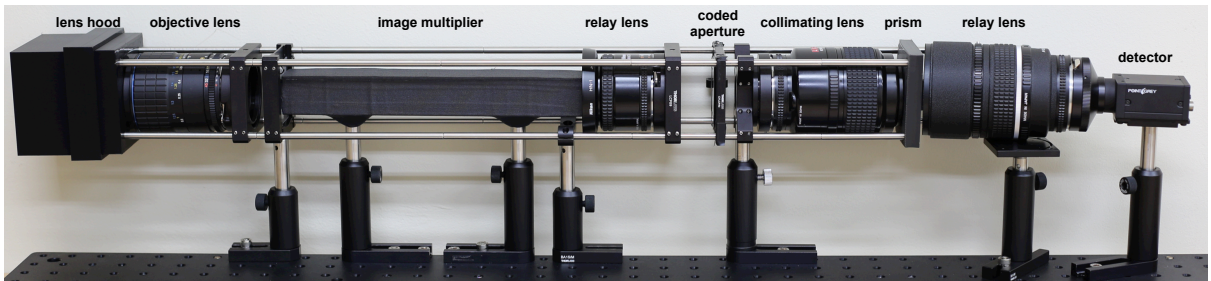


Figure 5.2: Hardware prototype of our hyperspectral imager. For actual operation we fully encapsulate the entire system by a 3D-printed cover hood to block interfering light.

Note that the halves of the duplicated views, on the main diagonal and anti-diagonal excluding the center one, are duplicated from their horizontal neighbors, and the other halves come from the vertical neighbors. For instance, the top-left view is a mixture of the top-mid and mid-left views. Since these views suffer from black diagonal line artifacts, which originate from the gap between two orthogonal first-surface mirrors (see Figure 5.5a), we use five views for our experiments, the original center and its four directly neighboring views.

We adjust the minification ratio of mirrors to configure 3×3 views of duplication. Figure 5.5 shows flipped duplication by mirrors. These changes of view orientations are initially calibrated by calculating a homography transform per each view \mathbf{g}_k . This initial transformation registers duplicated views to



Figure 5.3: Building the kaleidoscope. (a) presents a 3D model of our kaleidoscope holder, and (b) shows constructed kaleidoscope using four first-surface mirrors with two holders.

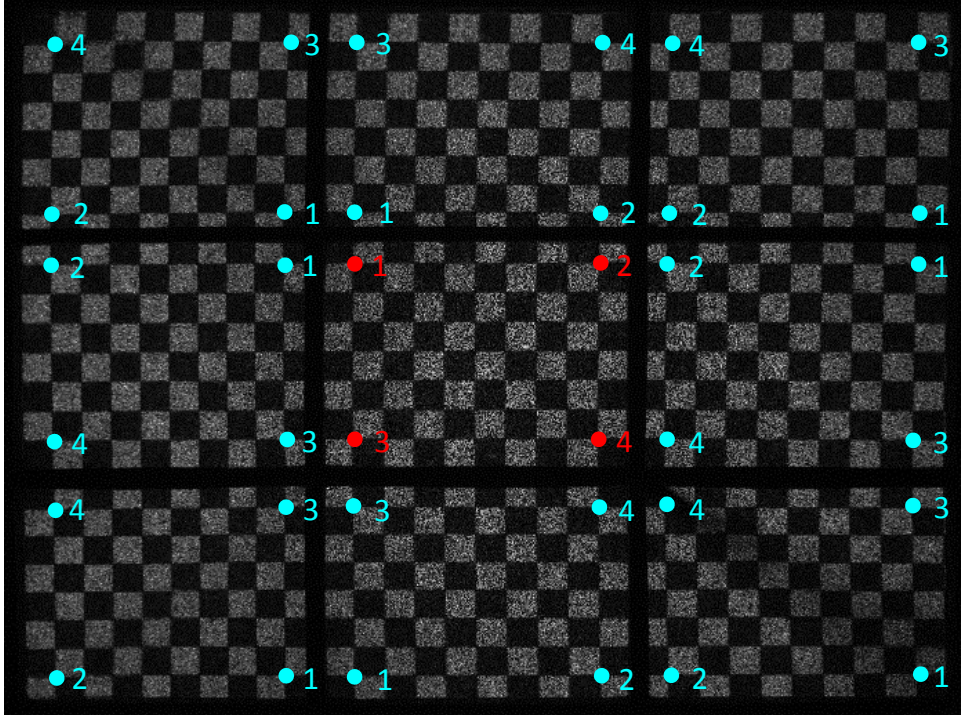


Figure 5.4: Detecting correspondance points from each view. The homography matrices can be computed from detected points.

the center view \mathbf{g}_0 in Equation (4.5). We then refine per-pixel registration in \mathbf{g}_k by applying optical flow [27]. Figure 5.5(a) presents a captured image of multiple views. Figure 5.5(b) shows direction changes of spectral dispersion in multiple views, following the kaleidoscopic imaging theory[39]. Our homography transformations include these direction changes of spectral dispersion.

5.1.4 Dispersion Directions

One of the insights of our optical design is that our mirror configuration diversifies the directions of dispersion of the coded aperture. The \mathbf{H}_k matrices in Equation (4.5) are flipped along the vertical axis, as shown in Figure 5.5. This allows more robust reconstruction of the horizontal dispersion while solving the inverse problem.

5.2 Radiometric Calibration

The camera response function of our hyperspectral imager can be described as the linear product of the sensor’s quantum efficiency \mathbf{q} and the overall light efficiency \mathbf{e} of the optical system. We then define the reconstructed signals \mathbf{f} of each wavelength in Equation (4.6) as $\mathbf{f} = \mathbf{qe}\mathbf{l}$, where \mathbf{l} is the radiance measured by the system. By determining a linear transformation $\mathbf{c} = (\mathbf{qe})^{-1}$, we can convert raw signals \mathbf{f} to incident radiance \mathbf{l} . To derive this calibration model, we captured and measured 24 colors in a standard color target (X-rite ColorChecker) to regress model coefficients using least squares. The multiplication of \mathbf{c} and \mathbf{f} yields physically-meaningful radiance \mathbf{l} from the reconstructed signals \mathbf{f} .

Once we obtain a hyperspectral radiance map, we convert it to sRGB color vectors to visualize visible spectral information as an sRGB color image. We first project spectra \mathbf{l} to tristimulus values of CIEXYZ using the CIE color matching functions \mathbf{M}_{XYZ} of 2-degree observation [7] following [21].

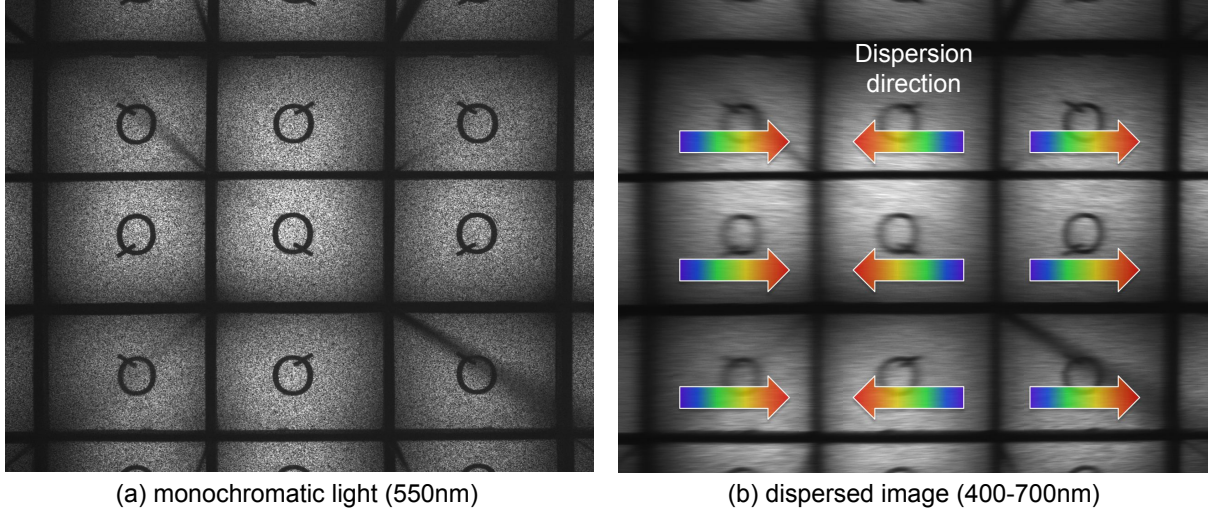


Figure 5.5: (a) A multiview image of a printed letter at a wavelength of 550 nm. Neighboring views are flipped vertically and horizontally. (b) The dispersion direction of the first and the third columns is from the blue (left) to red light (right), which is opposite to the direction of the second column.

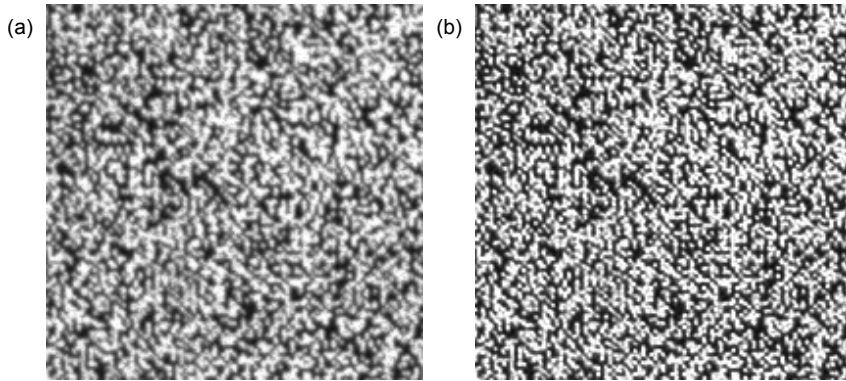


Figure 5.6: Overcoming the diffraction limit. (a) presents the raw capture of the aperture, and (b) shows the result of the deconvolution method.

We then transform the tristimulus values to sRGB color vectors \mathbf{s} using the standard sRGB transform \mathbf{M}_{sRGB} [34]: $\mathbf{s} = \mathbf{M}_{sRGB}\mathbf{M}_{XYZ}\mathbf{1}$. Finally, we apply a white balancing algorithm [3] to \mathbf{s} via gamma correction ($\gamma=2.2$) to obtain sRGB color images.

5.3 Technical Specifications

We implemented our design as the prototype shown in Figure 5.2. Our system consists of four lenses, four first-surface mirrors, a diffuse screen, a coded mask, a prism, and a monochromatic camera. This section provides technical specifications for hardware implementation.

5.3.1 Coded Aperture

A pixel in the coded aperture with random binary patterns corresponds to two-by-two pixels of the CCD camera, PointGrey Grasshopper 3 (9 megapixels with the resolution of 3376×2704). The spatial resolution of the mask patterns is critical to that of the output spectra. Although smaller features would yield a higher resolution, we also must consider the diffraction effect with smaller features. Owing to

the diffraction limit of the system, the coded aperture is blurred, as shown in Figure 5.6(a). In order to overcome the diffraction effect, we apply the Richard-Lucy deconvolution method [28] to the captured coded aperture mask image. This deconvolved image is used to build a matrix \mathbf{H} in Equation (4.6). Airy disk is the first order diffraction pattern of a circular aperture. The radius of the Airy disk kernel R is calculated by

$$R = k \frac{L\lambda}{d}, \quad (5.1)$$

where L is the distance from the camera aperture to the sensor plane, λ is the wavelength of light and d is the diameter of the camera aperture, and the constant $k = 1.22$ accounts for the shape of our circular aperture. The approximated size of the Airy disk α varies from $0.68 \mu\text{m}$ to $2.27 \mu\text{m}$ when the light of wavelength λ from 300 nm to $1,000 \text{ nm}$ comes via the iris, of which the size d is 25 mm . Since the pixel pitch of the employed CCD sensor (Sony ICX814) is $3.69 \mu\text{m}$, the estimated Airy disk size in our system is smaller than the pitch of a single pixel. The overall transmittance of this coded mask is $\sim 50\%$ as 50% of the mask area is occluded by chrome mask on quartz, where the pixel pitch of the coded mask is $7.40 \mu\text{m}$.

The approximated size of the Airy disk α varies from $0.68 \mu\text{m}$ to $2.27 \mu\text{m}$ when the light of wavelength λ from 300 nm to $1,000 \text{ nm}$ comes via the iris, of which the size d is 25 mm as follow: $\alpha \approx 2.44 \frac{L\lambda}{d}$, where L is the distance between the iris aperture and the sensor plane.

5.3.2 Spectral Dispersion

We mount a UV-IR cut filter to select incident spectral energy, wavelengths ranging between 450 nm and 700 nm . A solid-state plasma light source (Thorlabs HPLS-30-04) was used as a light source. Suppose we target reconstruction of about 30 wavelength channels of 10 nm intervals from a 2:1 ratio of the mask and the sensor pixel sizes in our system. The pixel range of spectral dispersion must span at least 60 pixels for visible spectra from 450 nm to 700 nm . We choose a prism made of BK-7. The refractive index of the material is 1.5168 . To fit our measurement goal, we fabricate the apex angle of the prism as 17° . See Figure 5.7 for the measured dispersion of visible spectra.

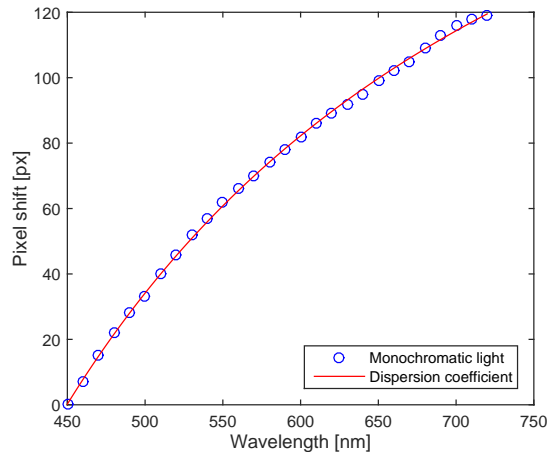


Figure 5.7: Measured dispersion coefficients of the prism.

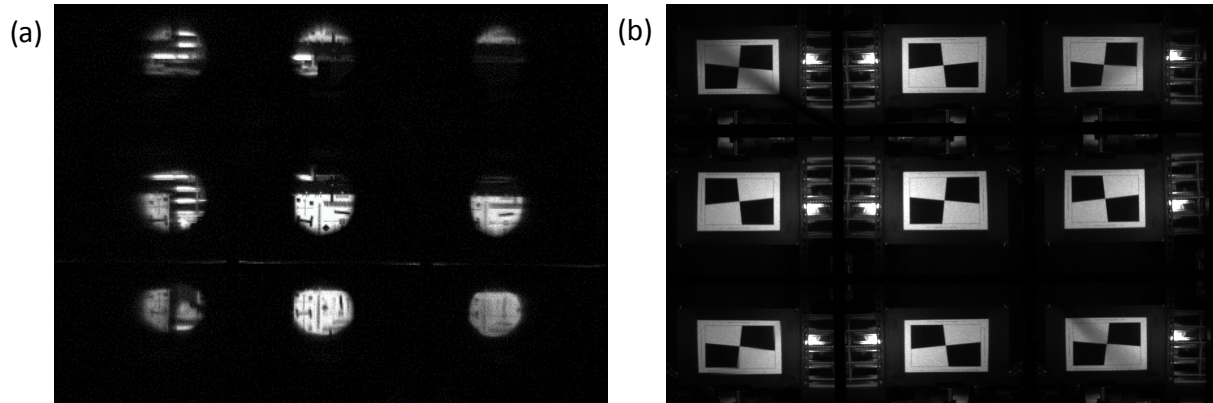


Figure 5.8: Effect of the diffuser: without diffuser (left), with diffuser (right). Without diffuser, most of the image is vignetted out.

5.3.3 Diffuse Screen

We install a diffuse screen at the focal length of the objective imaging lens to duplicate an image with four neighboring mirrors. A diffuser prevents rays at the corners of duplicated images from escaping away from the optical system. Without the diffuser, a severe vignette problem occurs as shown in Figure 5.8(a). We tested three types of diffusers: a ground glass and an opal and a holographic diffuser. The ground glass diffuser degrades image quality by grain and the opal diffuser shows very low transmittance. We therefore decided to use a holographic diffuser, the transmittance of which is specified as $\sim 85\%$ (Edmund Optics holographic diffuser #55-440).

5.3.4 Objective and Relay Lenses

We install a Coastal Optics 60 mm $f/4$ UV-VIS-IR lens as an objective lens that is apochromatic from approximately 315 nm to $1.1 \mu\text{m}$. We employ three Nikon lenses for optics relaying and imaging. In particular, the second lens from the left serves as an imaging lens, and the third one functions as a collimating lens by configuring the focal distance to infinity in these lenses. The ratio of the focal lengths of these lenses determines the zoom factor of our imaging system. We use the lenses of the same focal length of 50 mm to preserve 1:1 imaging.

Chapter 6. Results

In this chapter, we validate our multisampling compressive video spectroscopy by presenting a series of quantitative and qualitative analysis of experiment results. The experiments include evaluations via synthetic hyperspectral images and via real images captured by our imager. We reconstructed hyperspectral video footage using non-optimized Matlab codes. The reconstruction process for one frame (645×501) took approximately 200 seconds by a machine with an Intel i7-3770 CPU 3.4 GHz with 32 GB memory. Refer to the supplemental video for video results.

6.1 Reconstruction Accuracy

Here we validate the effectiveness of our multisampling design by simulating the reconstruction process, described in Section 4, with hyperspectral image datasets of the real world [54, 6]. The reference images are scaled to the same size as the employed sensor resolution. The active sensing area is segmented to nine views. We compare reconstruction results from five different multisampling configurations of 1/2/3/5/9 views with the reference hyperspectral image in terms of the peak signal-to-noise ratio (PSNR) and structural similarity (SSIM) [51].

Figure 6.1 validates that our multisampling design improves not only the spatial resolution (a) but also the accuracy of spectral measurements (b), as we increase input randomness. Figure 6.1(b) compares the differences between the reference measured by a calibrated spectroradiometer (Jeti Specbos 1200) and the reconstructed spectral reflectance over the red and the cyan patch, varying the number of input views. Figure 6.1(c) shows the averaged differences between the reference and the reconstructed radiance over the red and the blue patch. This experiment validates that as the number of input frames increases, the accuracy of the reconstructed hyperspectral images increases consistently. We also test the performance of our multisampling approach with 11 reference hyperspectral images [54] by comparing the reference and the reconstructed images. See Figure 6.1(d). The averaged PSNRs and SSIMs of reconstructed hyperspectral channels are improved consistently as the number of input views increases.

6.2 Multiview Tradeoff

The proposed method produces multiviews on a camera sensor by segmenting the sensing area into nine windows of 3×3 views. This means that we utilize nine times more samples than a single-frame CASSI in theory. On the other hand, this design reduces the spatial resolution of the reconstructed image (645×501) by $1/9^{th}$, compared with the traditional CASSI [45] (1935×1503) with the same hardware resources. Now we compare the two different design configurations under the same resources.

Figure 6.2(a) shows a hyperspectral image, synthetically reconstructed from a single image input of a traditional CASSI method [45]. The image resolution in the tradition CASSI is nine times higher than that of our nine-view configuration, while the remaining optical configurations such as the dispersion power are the same. Figure 6.2(b) presents a reconstruction result using a single subview among nine duplications in our method. Since the resolution of the input image is reduced by nine times compared to the original, it is not surprising that our reconstruction using a single view is worse than the full-frame reconstruction.

As shown in Figure 5.1(b), the spectral dispersion of these columns is inverted due to the design of kaleidoscopic imaging after image registration. We conduct a simulation to compare this effect of *dispersion inversion* in reconstructing the spectrum. Figures 6.2(c) and (d) compare results reconstructed from the five subviews without and with *dispersion inversion*. It is worth noting that although the number of input subviews is the same, the spatial resolution with dispersion inversion increases relatively in terms of the PSNR and SSIM of reconstructed hyperspectral channels. The configuration presented in Figure 6.2(d) is the one that we finally chose for our system implementation.

We implemented the traditional CASSI method [45] and the optical design described in Section 4.1 as our system prototype (Chapter 5). Note that we implemented both systems using the same hardware configuration just except the kaleidoscope unit. The traditional CASSI system captures images with nine times higher resolution than our proposed imaging system of nine subviews. Figure 5.1 shows a photograph of the system prototype. Figures 6.3(a) and (b) compare the hyperspectral images captured by the two imaging systems. It is not surprising that the traditional CASSI can provide a higher spatial resolution than the proposed method. However, comparing the reconstructed spectral resolutions from both systems, the spectral reflectance captured by our multisampling imager is significantly more accurate than the traditional CASSI system with the same hardware resource. Figures 6.3(c), (d) and (e) compare spectral reflectances of the blue, the green and the red patch, measured by both systems, with respect to reference measurements (Jeti Specbos 1200 spectroradiometer).

Figure 6.4 presents a hyperspectral video footage of a moving object of a color wheel. Refer to the supplemental video for more results. Figure 6.4(a) shows an example of a raw input frame for hyperspectral video captured by the system prototype (10FPS). Among nine multiviews we choose five clean views as input for spectral reconstruction due to diagonal artifacts. The yellow rectangles indicate the used frames. We then reconstruct them as a frame of the hyperspectral video footage, which contains per-pixel spectra in the 4D hyperspectral video footage (x, y, λ, t) . Figure 6.4(b) presents visible color visualization converted from reconstructed hyperspectral data. The right-hand-side array of photographs shows individual spectral channels. Figure 6.5 compares the quality of the reconstructed videos with different numbers of multiviews. We quantitatively evaluated the measurement accuracy by comparing our image-based measurements with spectroradiometer measurements. For instance, the measurement differences of the red sector in Figure 6.5 between our system and the spectroradiometer decreases by 21, 19, 18, and 10 in ΔE_{00}^* gradually as we increase the number of input views. Figure 6.6 shows four channels of the reconstructed spectral image. The multiview method produces spatially consistent images through each bandwidth, resulting in reduced rainbow effects on edges of objects. Figure 6.7 compares more hyperspectral video footage captured by our prototype. Refer to the supplemental video for more results.

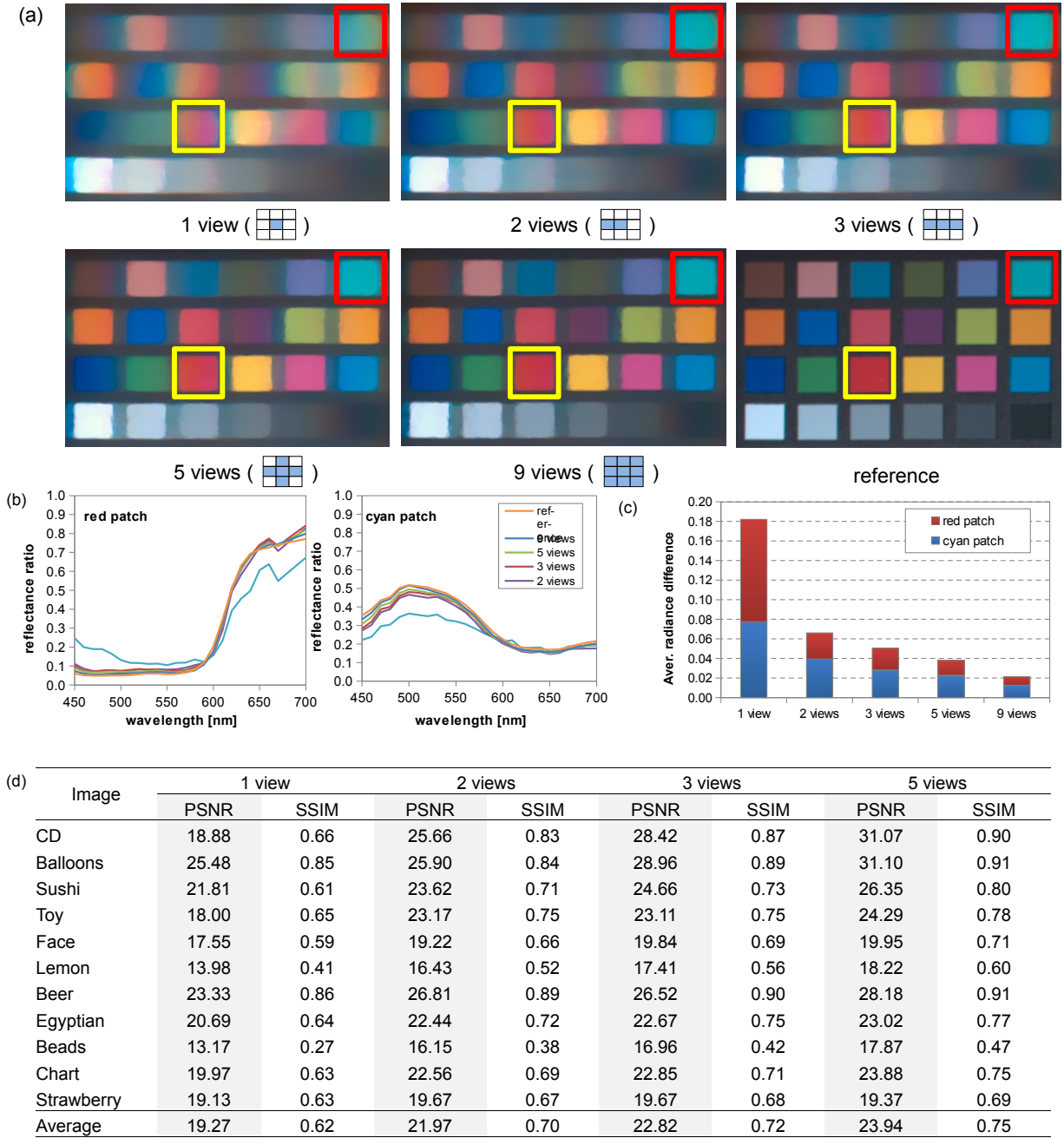


Figure 6.1: Comparison of hyperspectral images (a) and spectral measurements (b), synthetically reconstructed with different numbers of input views. The PSNRs of the reconstructed results from 1/2/3/5/9 views are 15.93/18.62/18.99/20.96/24.96. (b) compares the measurement accuracy of our method on the red and cyan patches by varying the number of input views. (c) compares the averaged radiance differences between the reference and the reconstruction of the red and cyan patches as the number of views increases. (d) compares the PSNRs and SSIMs between the reference [54] and the synthetically reconstructed hyperspectral images with different numbers of views. We used $\tau = 0.15$, and took 50 iterations for TV-L1 optimization.



Figure 6.2: (a) The traditional CASSI system [45] synthesized with a full-frame input (1935×1503), which has a nine times larger resolution than that of a view (645×501) in our multiview configuration. (b) a reconstruction result using a single view of the multiview configuration. (c) and (d) compare spectral reconstruction results using five different views that we use with our prototype. (c) shows a reconstruction result without dispersion inversion (see Figure 5.1b), while (d) presents a reconstruction results with dispersion inversion. The five-view reconstruction with dispersion inversion improves not only PSNR but also SSIM of spectral channels.

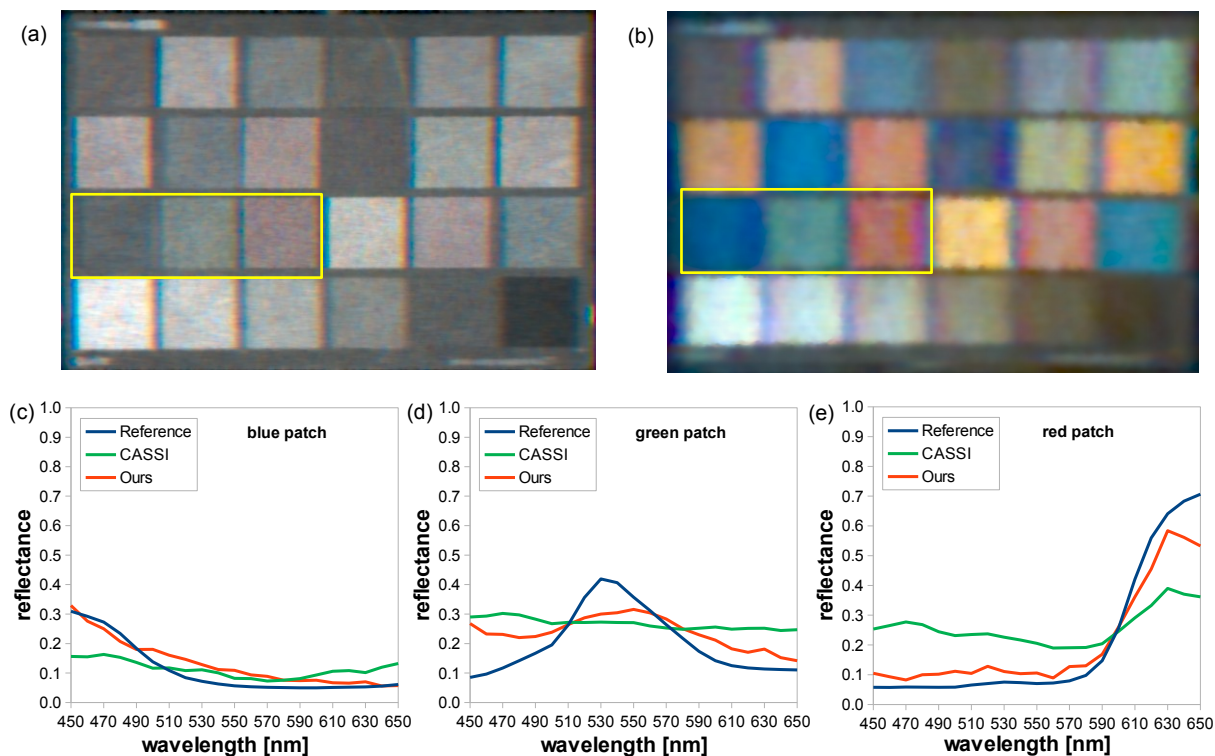


Figure 6.3: We compare the reflectances of color patches in a ColorChecker target measured by a spectroradiometer (Jeti Specbos 1200), a traditional CASSI system [45] and our system. (a) shows a hyperspectral image of the target captured by the traditional CASSI system. (b) shows a hyperspectral image captured by our system. (c), (d) and (e) compare the reconstructed spectral reflectance of the blue, the green and the red patch in the target using three instruments. Even though our system’s spatial resolution is lower than the traditional CASSI system, the accuracy of spectral reconstruction is significantly improved in our system.

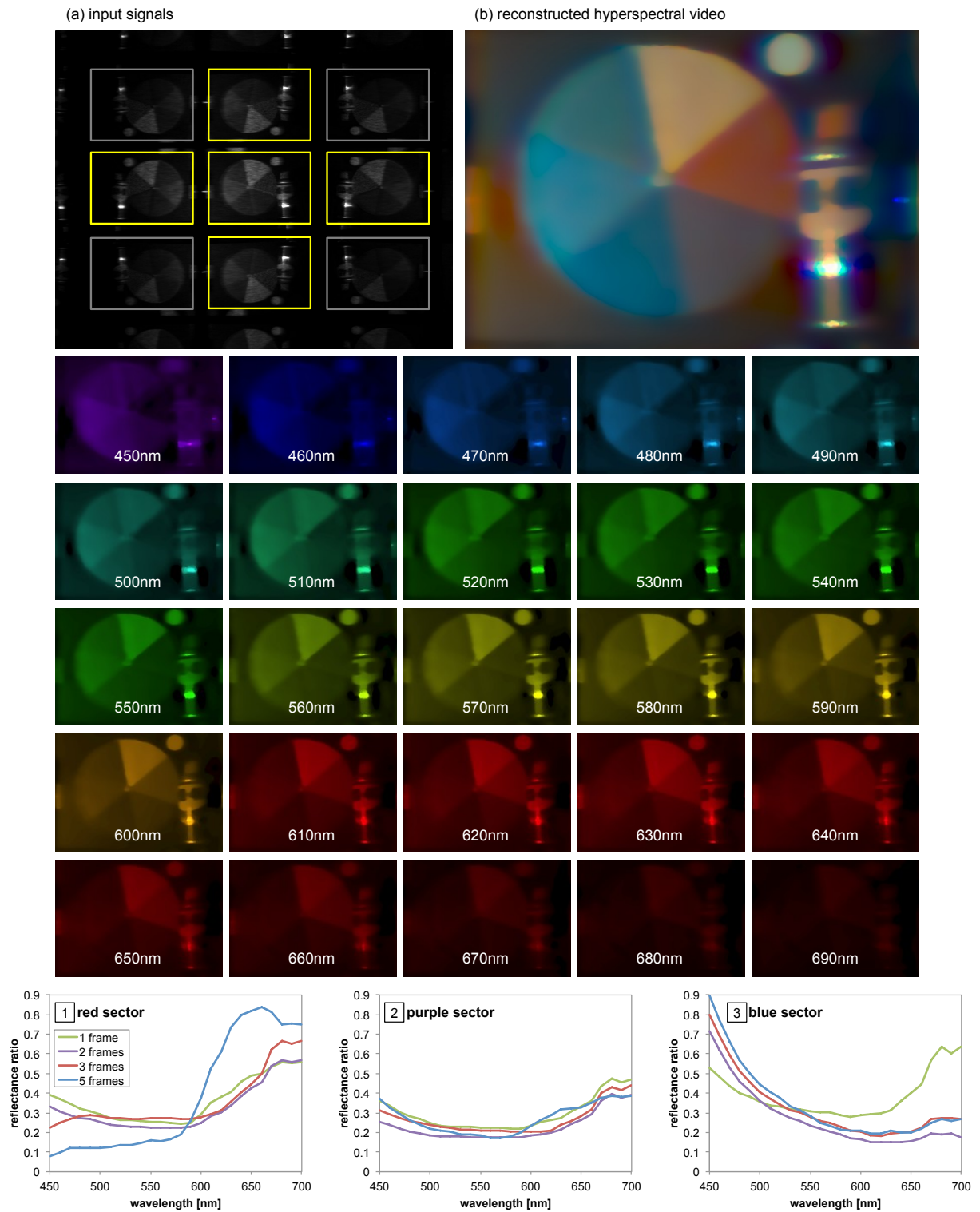


Figure 6.4: We captured hyperspectral video footage using our prototype. (a) shows the raw input of a single frame, where the yellow rectangles indicate the subviews that we used for reconstruction. (b) presents the sRGB color visualization of the reconstructed spectral channels from 450 nm to 700 nm in 10 nm intervals. The right-most image array presents the spectral power distributions of each wavelength in the video footage. Refer to the supplemental video for more results.

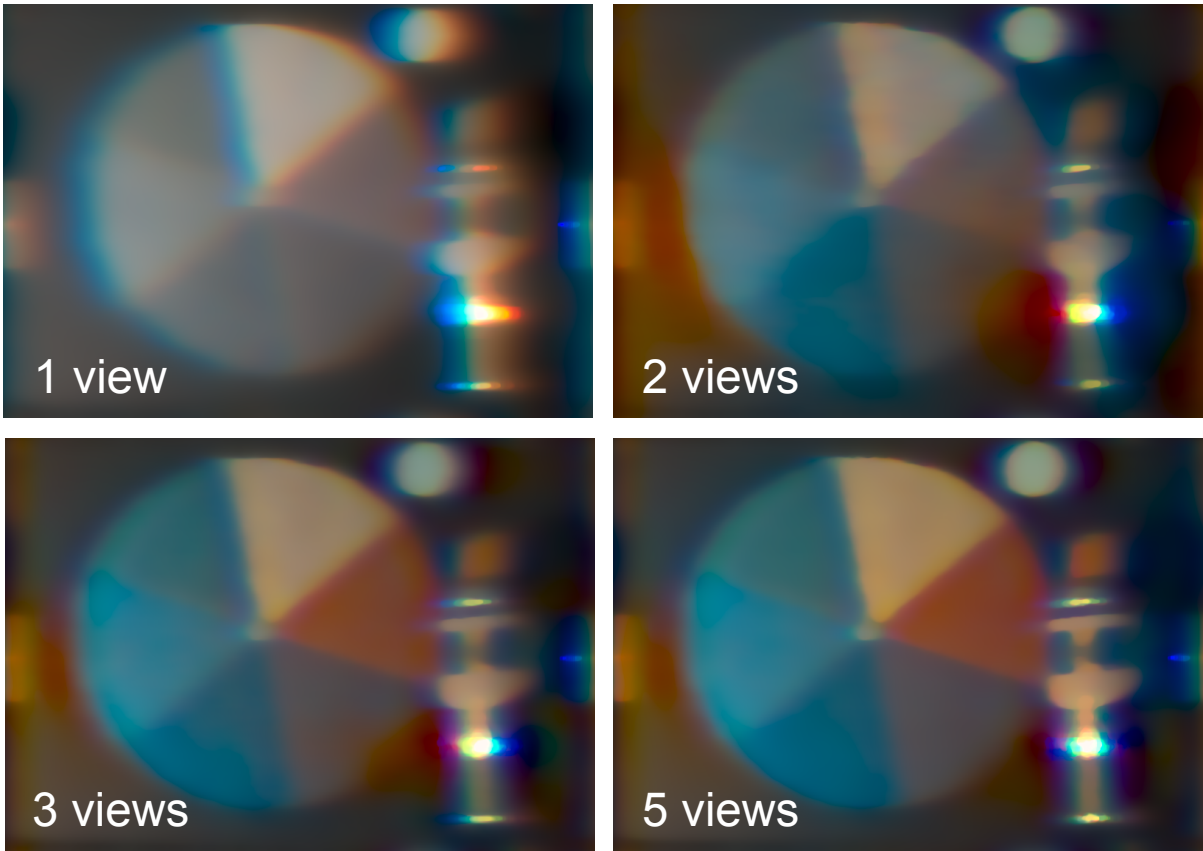


Figure 6.5: Reconstructed hyperspectral video footage with 1/2/3/5 multiviews, captured by our prototype.

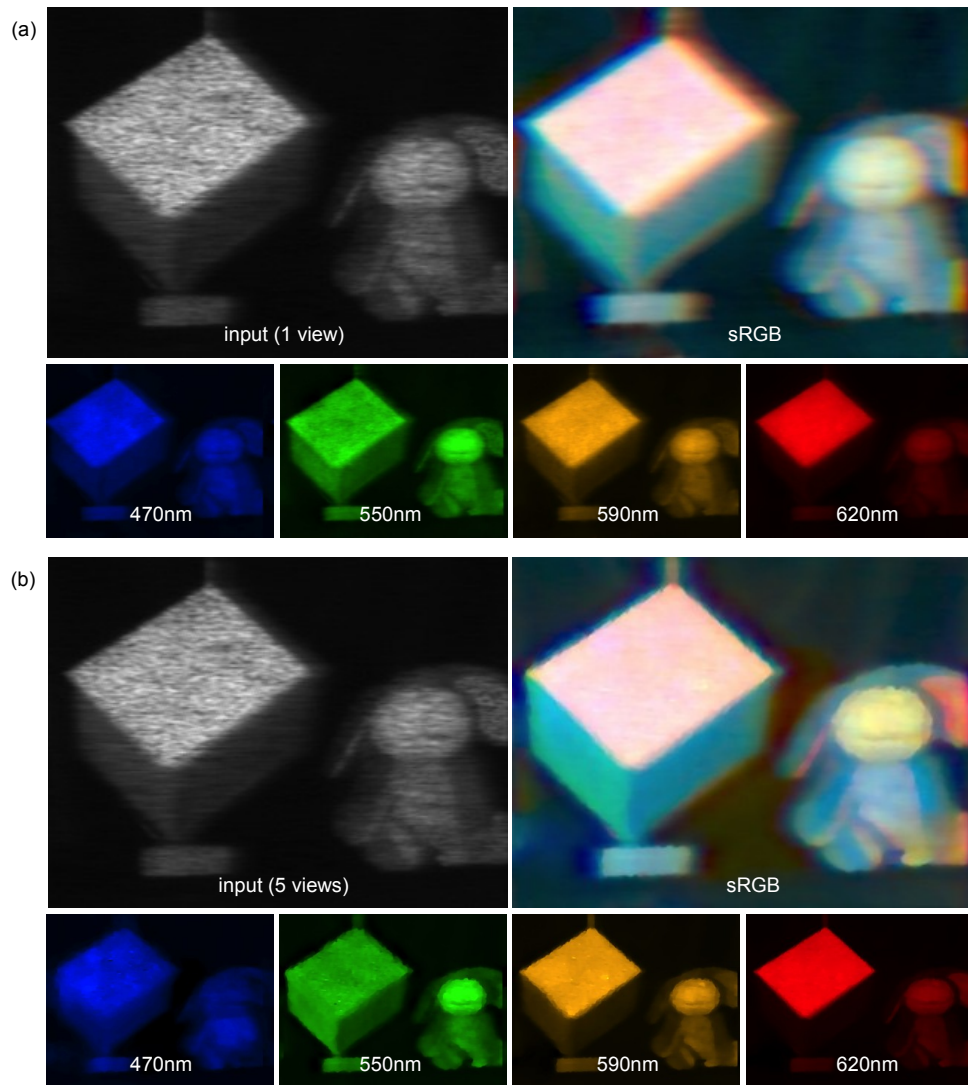
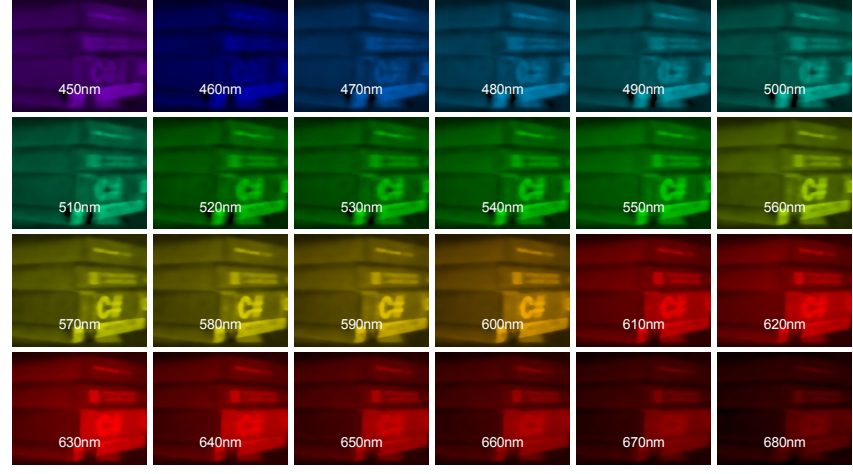
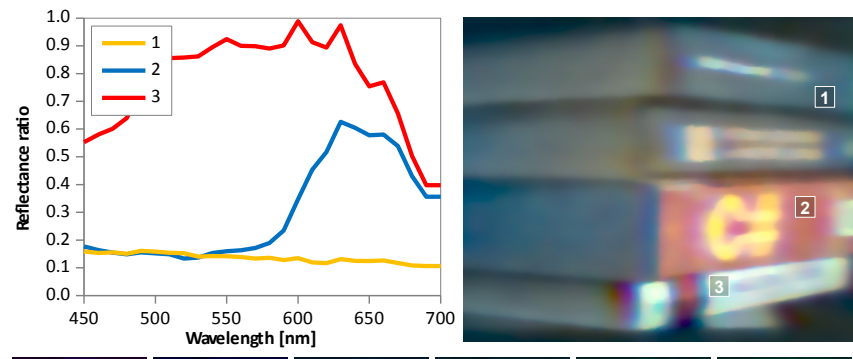
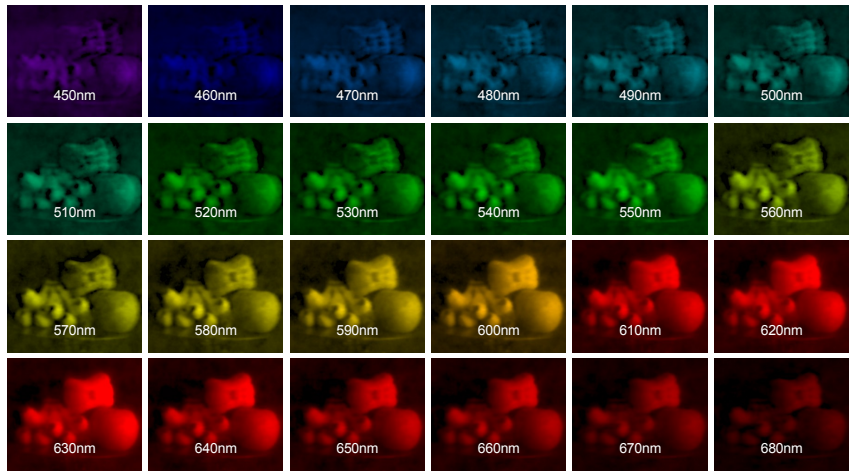
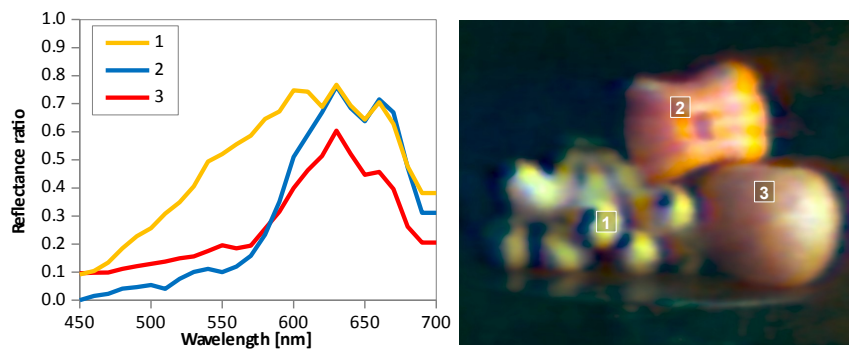


Figure 6.6: We compare reconstructed sRGB images and spectral channels of 470/550/590/620 nm captured by our system prototype. (a) shows 1 view result, and (b) presents 5 multiview result.



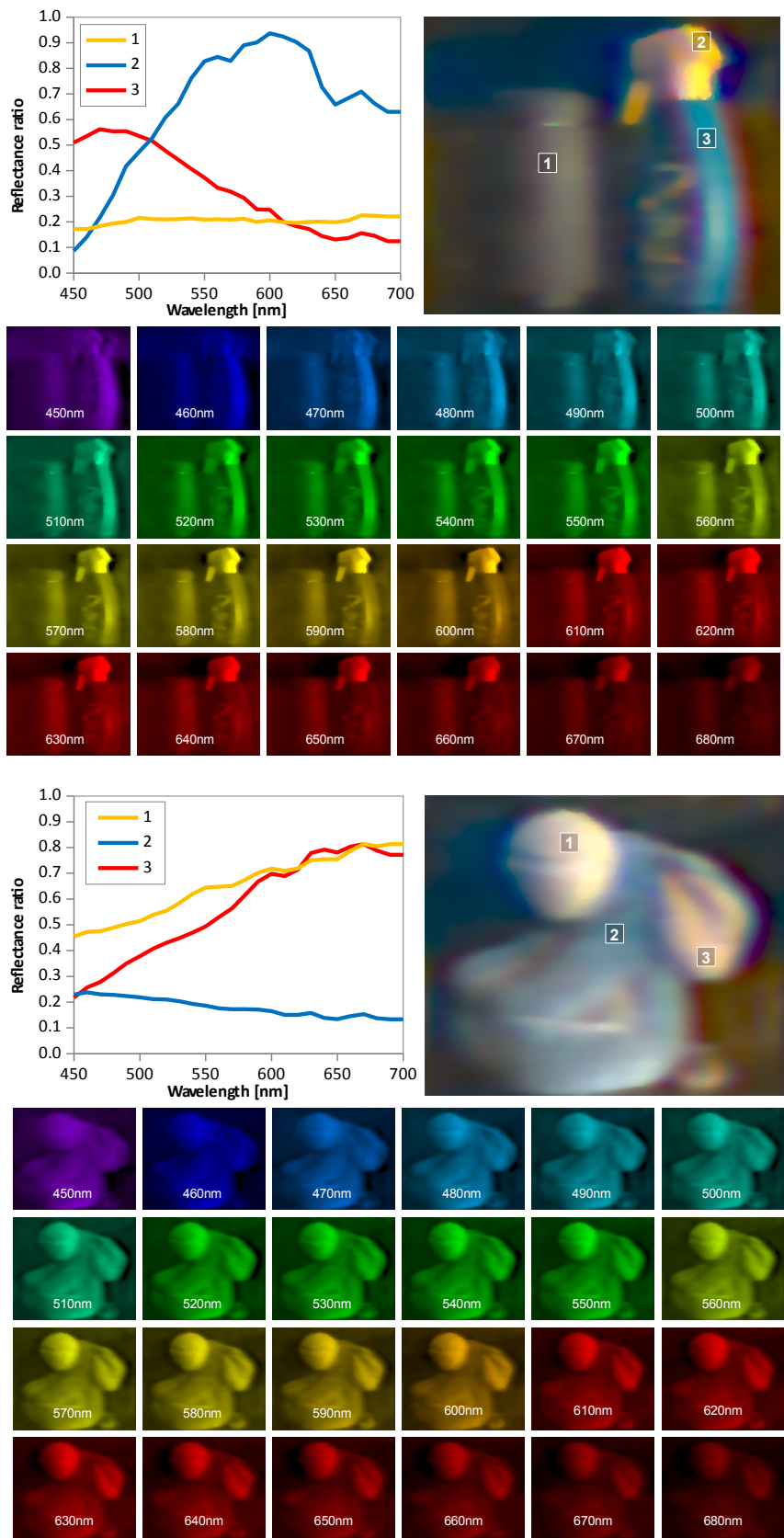


Figure 6.7: We captured hyperspectral video footage using our system prototype. This figure presents measured reflectances, sRGB color images and spectral channels of moving objects. Refer to the supplemental video for more results.

Chapter 7. Discussion and Future Work

We discuss a range of observations made throughout the development of our system and the acquisition of a variety of test scenes.

Tradeoff between Spatial and Spectral Resolution. Filter-based approaches [30] provide high-spatial resolution, but their spectral resolution is limited. Compressive imaging approaches [26, 25] including the proposed method provide high-spectral resolution, but their spatial resolution is limited. This is a long-lasting tradeoff between spatial and spectral resolution in hyperspectral imaging. Many approaches to solving this tradeoff [22, 53] by combining multiple sampling and compressive imaging have been proposed. Compressive imaging principles stand on sparsity, randomness, and convex optimization. The solution of this problem that we propose is multiple sampling of the randomness of sparse modulation of the spectrum using kaleidoscopic imaging. The proposed method accommodates multiple sampling and video imaging. We demonstrate increased sampling of randomness is beneficial to enhance spectral resolution significantly, despite that we utilize the entire sensor resolution partially as segments via a kaleidoscope.

Randomness of the Coded Mask. Regarding compressive sensing, it is well documented that randomness leads to an effective sensing mechanism in reconstructing sparsely sampled signals. We create random patterns by lithographically etching a quartz substrate with an active area of 25 mm square, where a pixel on the mask corresponds to 2-by-2 pixels on a sensor. The key insight is that the randomness provides incoherence in sampling sparse signals, which is crucial for sparsity-based optimization such as total-variation or sparse coding. In the compressive sensing field, random sensing is practiced as a near-optimal strategy.

Hardware Assembly. As shown in our experimental results, the spatial resolution captured by our prototype is noticeably lower than the synthetic results. We found that building the prototype requires sophisticated alignment of optical components including the coded aperture, the four mirrors, the prism, and the camera along the optical path. The diffraction effect through the coded mask and lens distortion, which is not present in the synthetic experiments, hindered sharp reconstruction of captured spectra. We notice that the misalignment of copied views gives rise to a critical reconstruction problem. Although the misalignment can be solved by image registration, the dispersion directions of each view are different due to misaligned orientation of views. Distortion of dispersion directions breaks the transformation matrix and corrupts the hyperspectral image reconstruction. Also, focusing on the coded mask contributes to the quality of reconstructed images. Since fine focusing requires perfect lenses and high precision positioning, we obtain a slightly blurred image of the coded mask.

Implementation of Kaleidoscope. Designing a system to use nine views originally, we found that even small corner seams near four edges of the mirrors hindered reconstruction of sparse information, as shown in the diagonal views in Figure 5.5(a). Owing to this issue in fabricating the mirror holder, we omitted these corner views from multiple sampling in the system. Eventually, qualities of the results drop, since we only used five views out of nine views. However, a more elaborately fabricated mirror holder would solve this problem.

Dispersion Power. Dispersion power of dispersive unit influences spectral and spatial resolution of the results. A system with high dispersion has advanced wavelength isolation capability but causes large overlapping among dispersed light. Consequently, the results came with improved spectral resolution

and decreased spatial resolution. The prism used in our system, which has apex angle of 17° , provides too high dispersion power. Our target number of bands is 25, but pixel shift difference of 450nm and 750nm is 120. Due to high dispersion, spatial resolution of the system is lower than expected. A prism with one-third dispersion power would be enough for our target spectral resolution.

Spatial Coding vs. Spectral Coding. Two types of CASSI has been introduced: a single-disperser CASSI (SD-CASSI) and a dual-disperser CASSI (DD-CASSI). In the SD-CASSI, the spectral data cube is sheared after passing through a coded aperture. In the DD-CASSI, the spectral data cube is sheared before passing through a coded aperture, and the cube is sheared again to original shape after coded aperture. As a result, the SD-CASSI encodes spatial data, and the DD-CASSI encodes spectral data of the input cube. The dual CASSI is more complex than the single CASSI because the dual CASSI needs one more image relaying. Also shearing back to original shape causes a difficult aligning problem. For these reasons, we selected SD-CASSI for our system. However, we found that pixel overlapping along wavelengths reduced the spatial resolution of the results. Moreover, local optimization algorithms are unable to solve the problem due to pixel shifting. Recent works [26, 25] achieve spectral coding using a single dispersive unit by modifying DD-CASSI system. In future work, we are planning to choose the DD-CASSI for our system design to improve performance of the imaging system.

Dispersion Direction. An unexpected advantage of the kaleidoscope multiview system is inverted dispersion direction of side views. Coded data with different dispersion directions leads to more robust reconstruction by measuring data with various light modulation. Using more number of diffraction directions would improve performance of the system. The computed tomography imaging spectrometer [11, 15] have been already utilized various dispersion directions using a cross diffraction grating. The first mode of the cross diffraction grating creates dispersed images with eight directions. Combining coded aperture spectroscopy and computed tomography is a possible research topic for enhanced hyperspectral imaging.

Light Efficiency. In traditional CASSI systems, the coded mask occludes 50% of incident light to yield spatial modulation. In state-of-the-art imaging systems with multiple cameras [49, 50], a beam splitter is necessary to divide incident light into two directions with a further 50% loss, i.e., this configuration leads to a combined 75% loss of incident energy on the camera equipped with the coded aperture. In contrast, our mirror-based multisampling approach enhances spectral resolution with a cost of only 15% loss of incident energy by the diffuser.

TV-L1 Optimization vs. Sparse Coding. Traditional CASSI reconstruction methods [14, 45, 22, 53] formulate the reconstruction problem as an inverse problem that minimizes $\|\mathbf{g} - \mathbf{H}\mathbf{f}\|_2^2$ with TV-L1 including our method (refer to Equation (4.6)). Recent reconstruction methods using sparse representation such as [26, 25, 35, 50] formulate this problem as minimizing $\|\mathbf{g} - \mathbf{\Phi}\mathbf{D}\boldsymbol{\alpha}\|_2^2$, where $\mathbf{\Phi}$ is a projection matrix, \mathbf{D} is a 3D spatio-spectral dictionary, and $\boldsymbol{\alpha}$ is a corresponding sparse code vector. This over-complete dictionary \mathbf{D} is learned from a large set of 3D spatio-spectral patches. While the former methods solve the optimization problem with a *global* spatio-spectral matrix \mathbf{H} , the latter approaches solve the *local* optimization problems with a large set of independent spatio-spectral dictionaries. These sparse coding-based approaches require many hours for training and even reconstruction; e.g., it takes 25 hours to reconstruct an image of 374×502 pixels by a state-of-the-art method [25]. Since we are targeting video applications of spectroscopy, we were motivated to choose the traditional reconstruction approach with consideration of computational cost. We tested five methods: TWIST [1], GPSR [10], NeARest [42], SpARSA [52], and a sparse coding approach [26]. We chose TWIST because it is the most efficient and accurate. In future work, we would like to apply a sparse coding-based approach to solving the opti-

mization problem. Recently, performance of deep learning technology has been significantly increased. Instead of solving optimization problem in the reconstruction stage, deep learning with convolution kernel on image through network. The simple reconstruction computation allows fast speed. Other computer vision applications [8, 44] prove that deep learning produces results with better quality than existing solutions in shorter time. Deep learning is an alternative approach to overcome high computational cost of reconstruction.

Chapter 8. Conclusion

We present a novel camera system for compressive imaging to measure hyperspectral video. We make a tradeoff between multi-sampling (beneficial for spatial and spectral resolution, which hinders video acquisition) and snapshot-based design (beneficial for hyperspectral video acquisition, which suffers from low spatial resolution) by combining a coded aperture and a kaleidoscope to achieve high spatial and spectral resolution in hyperspectral videos. Specifically, we provide insights for coupling multisampling and compressive imaging, offering physically-meaningful acquisition of hyperspectral video. We validate the effectiveness and consistency of our system qualitatively and quantitatively. Finally, we provide a range of building experience and potential directions for compressive video spectroscopy.

Bibliography

- [1] J. Bioucas-Dias and M. Figueiredo. A new twist: two-step iterative shrinkage/thresholding for image restoration. *IEEE TIP*, 16(12):2992–3004, 2007.
- [2] D. J. Brady. *Optical Imaging and Spectroscopy*. Wiley-OSA, 2009.
- [3] G. Buchsbaum. A Spatial Processor Model for Object Colour Perception. *J. the Franklin Institute*, 310(1):1–26, 1980.
- [4] X. Cao, H. Du, X. Tong, Q. Dai, and S. Lin. A prism-mask system for multispectral video acquisition. *IEEE TPAMI*, 33(12):2423–2435, 2011.
- [5] X. Cao, X. Tong, Q. Dai, and S. Lin. High resolution multispectral video capture with a hybrid camera system. In *CVPR*, 2011.
- [6] A. Chakrabarti and T. Zickler. Statistics of Real-World Hyperspectral Images. In *CVPR*, 2011.
- [7] CIE. Colorimetry. CIE Pub. 15.2, Commission Internationale de l’Eclairage (CIE), Vienna, 1986.
- [8] C. Dong, C. C. Loy, K. He, and X. Tang. Learning a deep convolutional network for image super-resolution. In D. J. Fleet, T. Pajdla, B. Schiele, and T. Tuytelaars, editors, *ECCV (4)*, volume 8692 of *Lecture Notes in Computer Science*, pages 184–199. Springer, 2014.
- [9] H. Du, X. Tong, X. Cao, and S. Lin. A prism-based system for multispectral video acquisition. In *ICCV*, 2009.
- [10] M. Figueiredo, R. Nowak, and S. Wright. Gradient projection for sparse reconstruction: Application to compressed sensing and other inverse problems. *IEEE J-STSP*, 1(4):586–597, 2007.
- [11] B. Ford, M. Descour, and R. Lynch. Large-image-format computed tomography imaging spectrometer for fluorescence microscopy. *Optics express*, 9(9):444–53, 2001.
- [12] L. Gao, R. T. Kester, N. Hagen, and T. S. Tkaczyk. Snapshot image mapping spectrometer (ims) with high sampling density for hyperspectral microscopy. *Optics express*, 18(14):14330–44, 2010.
- [13] N. Gat and G. Scriven. Development of four-dimensional imaging spectrometers (4d-is). *Proc. SPIE*, 6302:63020M–63020M–11, 2006.
- [14] M. E. Gehm, R. John, D. J. Brady, R. M. Willett, and T. J. Schulz. Single-shot compressive spectral imaging with a dual-disperser architecture. *OSA OE*, 15(21):14013–27, 2007.
- [15] R. Habel, M. Kudenov, and M. Wimmer. Practical spectral photography. *Wiley CGF*, 31:449–458, 2012.
- [16] J. Y. Han and K. Perlin. Measuring bidirectional texture reflectance with a kaleidoscope. *ACM TOG*, 22(3):741–748, 2003.
- [17] J. Y. Hardeberg, F. Schmitt, and H. Brettel. Multispectral color image capture using a liquid crystal tunable filter. *Optical engineering*, 41(10):2532–2548, 2002.

- [18] G. Hoye and A. Fridman. Mixel camera – a new push-broom camera concept for high spatial resolution keystone-free hyperspectral imaging. *OSA OE*, 21(9):11057–11077, 2013.
- [19] R. Kawakami, J. Wright, Y.-W. Tai, Y. Matsushita, M. Ben-Ezra, and K. Ikeuchi. High-resolution hyperspectral imaging via matrix factorization. In *CVPR*, pages 2329–2336, 2011.
- [20] M. H. Kim, T. A. Harvey, D. S. Kittle, H. Rushmeier, J. Dorsey, R. O. Prum, and D. J. Brady. 3d imaging spectroscopy for measuring hyperspectral patterns on solid objects. *ACM TOG*, 31(4):38:1–11, 2012.
- [21] M. H. Kim, H. Rushmeier, J. French, I. Passeri, and D. Tidmarsh. Hyper3d: 3d graphics software for examining cultural artifacts. *ACM JOCCH*, 7(3):1:1–19, 2014.
- [22] D. Kittle, K. Choi, A. Wagadarikar, and D. J. Brady. Multiframe image estimation for coded aperture snapshot spectral imagers. *OSA AO*, 49(36):6824–33, 2010.
- [23] H. Lee and M. H. Kim. Building a two-way hyperspectral imaging system with liquid crystal tunable filters. In *ICISP*, pages 26–34, 2014.
- [24] A. Levin, R. Fergus, F. Durand, and W. T. Freeman. Image and depth from a conventional camera with a coded aperture. *ACM Transactions on Graphics*, 26(3):70:1–70:??, July 2007.
- [25] X. Lin, Y. Liu, J. Wu, and Q. Dai. Spatial-spectral encoded compressive hyperspectral imaging. *ACM TOG*, 33(6), 2014.
- [26] X. Lin, G. Wetzstein, Y. Liu, and Q. Dai. Dual-Coded Compressive Hyper-Spectral Imaging. *OSA OL*, 39:2044–2047, 2014.
- [27] C. Liu. *Beyond Pixels: Exploring New Representations and Applications for Motion Analysis*. Ph.D. Thesis, Massachusetts Institute of Technology, 2009.
- [28] L. B. Lucy. An iterative technique for the rectification of observed distributions. *The astronomical journal*, 79:745, 1974.
- [29] C. Ma, X. Cao, R. Wu, and Q. Dai. Content-adaptive high-resolution hyperspectral video acquisition with a hybrid camera system. *Optics letters*, 39(4):937–940, 2014.
- [30] A. Manakov, J. F. Restrepo, O. Klehm, R. Hegedüs, E. Eisemann, H.-P. Seidel, and I. Ihrke. A reconfigurable camera add-on for high dynamic range, multispectral, polarization, and light-field imaging. *ACM TOG*, 32(4):47, 2013.
- [31] A. Mansouri, A. Lathuiliere, F. Marzani, Y. Voisin, and P. Gouton. Toward a 3D multispectral scanner: An application to multimedia. *IEEE MultiMedia*, 14(1):40–47, 2007.
- [32] P. Mouroulis, R. O. Green, and T. G. Chrien. Design of pushbroom imaging spectrometers for optimum recovery of spectroscopic and spatial information. *Applied Optics*, 39(13):2210–2220, 2000.
- [33] G. Nam and M. H. Kim. Multispectral photometric stereo for acquiring high-fidelity surface normals. *IEEE CGA*, 34(6):57–68, 2014.
- [34] M. Nielsen and M. Stokes. The creation of the sRGB ICC Profile. In *CIC*. IS&T, 1998.

- [35] Y. Peng, D. Meng, Z. Xu, C. Gao, Y. Yang, and B. Zhang. Decomposable nonlocal tensor dictionary learning for multispectral image denoising. In *CVPR*, 2014.
- [36] A. Rajwade, D. Kittle, T.-H. Tsai, D. Brady, and L. Carin. Coded hyperspectral imaging and blind compressive sensing. *SIAM Journal on Imaging Sciences*, 6(2):782–812, 2013.
- [37] K. Rapantzikos and C. Balas. Hyperspectral imaging: potential in non-destructive analysis of palimpsests. In *ICIP*, volume 2, 2005.
- [38] I. Reshetouski, A. Manakov, A. Bhandari, R. Raskar, H.-P. Seidel, and I. Ihrke. Discovering the structure of a planar mirror system from multiple observations of a single point. In *CVPR*, 2013.
- [39] I. Reshetouski, A. Manakov, H.-P. Seidel, and I. Ihrke. Three-dimensional kaleidoscopic imaging. In *CVPR*, 2011.
- [40] H. Rueda, H. Arguello, and G. R. Arce. DMD-based implementation of patterned optical filter arrays for compressive spectral imaging. *OSA JOSAA*, 32(1):80–89, 2015.
- [41] A. Serrano, F. Heide, D. Gutierrez, G. Wetzstein, and B. Masia. Convolutional Sparse Coding for High Dynamic Range Imaging. *Wiley CGF*, 35(2), 2016.
- [42] X. Sun and N. Pitsianis. Solving non-negative linear inverse problems with the NeAREst method. *Proc. SPIE*, 7074:707402, 2008.
- [43] T.-H. Tsai and D. J. Brady. Coded aperture snapshot spectral polarization imaging. *OSA AO*, 52(10):2153–2161, 2013.
- [44] M. Waechter, N. Moehrle, and M. Goesele. Let there be color! large-scale texturing of 3d reconstructions. In *Computer Vision–ECCV 2014*, pages 836–850. Springer, 2014.
- [45] A. Wagadarikar, R. John, R. Willett, and D. Brady. Single disperser design for coded aperture snapshot spectral imaging. *OSA AO*, 47(10):B44–B51, 2008.
- [46] A. A. Wagadarikar, N. P. Pitsianis, X. Sun, and D. J. Brady. Spectral image estimation for coded aperture snapshot spectral imagers. volume 7076, pages 707602–707602–15, 2008.
- [47] A. A. Wagadarikar, N. P. Pitsianis, X. Sun, and D. J. Brady. Video rate spectral imaging using a coded aperture snapshot spectral imager. *OSA OE*, 17(8):6368–88, 2009.
- [48] L. Wang, D. Gao, G. Shi, and Y. Niu. Double-channel compressive spectral imaging via complementary code patterns. In *ICSPCC*, 2013.
- [49] L. Wang, Z. Xiong, D. Gao, G. Shi, and F. Wu. Dual-camera design for coded aperture snapshot spectral imaging. *OSA AO*, 54(4):848–858, 2015.
- [50] L. Wang, Z. Xiong, D. Gao, G. Shi, W. Zeng, and F. Wu. High-speed hyperspectral video acquisition with a dual-camera architecture. In *CVPR*, 2015.
- [51] Z. Wang, A. C. Bovik, H. R. Sheikh, and E. P. Simoncelli. Image quality assessment: from error visibility to structural similarity. *IEEE TIP*, 13(4):600–612, 2004.
- [52] S. Wright, R. Nowak, and M. Figueiredo. Sparse reconstruction by separable approximation. *IEEE TSP*, 57(7):2479–2493, 2009.

- [53] Y. Wu, I. O. Mirza, G. R. Arce, and D. W. Prather. Development of a digital-micromirror-device-based multishot snapshot spectral imaging system. *OSA OL*, 36(14):2692–4, 2011.
- [54] F. Yasuma, T. Mitsunaga, D. Iso, and S. Nayar. Generalized Assorted Pixel Camera: Post-Capture Control of Resolution, Dynamic Range and Spectrum. Technical report, Nov 2008.

Acknowledgments in Korean

이 석사학위 논문을 완성하기까지 많은 분들의 도움이 있었습니다. 학사 시절부터 연구 지도를 해 주시고 논문을 완성하기 위해 많은 도움을 주신 김민혁 교수님께 먼저 감사드립니다.

지금까지 저를 뒷바라지 해 주시고 여기까지 올 수 있도록 도와주신 아버지, 어머니께 감사드립니다. 또한 힘이 되어 준 든직한 우리 형도 고맙습니다.

같은 연구실에서 생활하면서 어려울 때 도움을 주고 여러가지 좋은 조언들을 전해준 VCLAB 식구들에게도 감사합니다. 믿음직스러운 인창이형, 연구실 장비 전문 길주형, 연구실의 활력소가 되어준 주호형, 연구 잘하는 승환이형, 자유로운 영혼의 영범이형, 사진작가 인철이형, 민군이형, 지금은 졸업한 가정적인 해봄이형 모두 감사합니다.

또한 4년 동안 기숙사 룸메이트로 살면서 동고동락해온 상연이에게 고마움을 전하고자 합니다. 그 외에도 광주과학고등학교 친구들, 인클루드 동아리 멤버들에게도 고맙습니다.

그리고 여기서 언급하지 못했지만 지금의 자리까지 오는데 도움을 주신 많은 분들에게도 감사의 말을 전합니다. 모두 건강하고 행복했으면 좋겠습니다.

Curriculum Vitae in Korean

이 름: 전 석 준
생 년 월 일: 1992년 5월 1일
출 생 지: 광주광역시 북구 용봉동 쌍용예가아파트 101동 305호
주 소: 대전 유성구 구성동 카이스트 전산학부 E3빌딩 3422호
전 자 주 소: sjjeon@vclab.kaist.ac.kr

학 력

2008. 3. – 2010. 2. 광주과학고등학교 (2년 수료)
2010. 3. – 2014. 8. 한국과학기술원 전산학과 (B.S.)

경 력

2014. 9. – 2016. 6. 한국과학기술원 전산학부 일반조교

연구 업 적

1. Daniel S. Jeon, Inchang Choi, and Min H. Kim, *Multisampling Compressive Video Spectroscopy*, Computer Graphics Forum (Proc. Eurographics 2016), May 12, 2016, 35(2), pp. 467–477.